Optimizing LOS/NLOS Modeling and Solution Determination for 3D-Mapping-Aided GNSS Positioning

Qiming Zhong, Paul Groves
University College London, United Kingdom

BIOGRAPHY

Qiming Zhong is a PhD student at University College London (UCL), specializing in 3D-mapping-aided GNSS. He holds a BSc in Electrical and Electronic Engineering from the University of Nottingham, Ningbo, China and an MSc in Robotics and Computing from UCL. (q.zhong.17@ucl.ac.uk)

Dr Paul Groves is an Associate Professor at UCL, where he leads a program of research into robust positioning and navigation. He is interested in all aspects of navigation and positioning, including multi-sensor integrated navigation, improving GNSS performance under challenging reception conditions, and novel positioning techniques. He is author of the book Principles of GNSS, Inertial and Multi-Sensor Integrated Navigation Systems. He is the recipient of the 2016 Institute of Navigation Thurlow Award and a Fellow of the Royal Institute of Navigation. He holds a bachelor's degree and doctorate in physics from the University of Oxford. (p.groves@ucl.ac.uk)

ABSTRACT

In urban environments, the propagation of satellite signals may be affected by buildings, resulting in poor performance of conventional GNSS positioning. Several studies have shown that 3D mapping data of buildings significantly improves GNSS positioning by predicting which signals are line-of-sight (LOS) and which are non-line-of-sight (NLOS). This study introduces several improvements to current UCL's 3DMA GNSS techniques, including enhanced satellite visibility prediction for overhanging structures, inclusion of untracked satellites for shadow matching to improve satellite geometry, Bayesian inference-based shadow matching adaptable to various densities of urban environments, a new NLOS model for likelihood-based ranging, and a region growing-based clustering algorithm to manage ambiguity. The effectiveness of these enhancements was validated using GNSS datasets collected in London, representing diverse urban scenarios. The results show that the enhanced 3DMA GNSS algorithm improves the RMS position error in the horizontal radial direction by more than 20% compared to the original version.

I. INTRODUCTION

Global Navigation Satellite Systems (GNSS), which include systems such as GPS, Galileo, Beidou, and GLONASS, play a crucial role in numerous applications ranging from navigation and timing to location-based services. Positioning modules receive satellite signals and derive location information. The positioning modules have benefited from their reduced size and cost and have been incorporated into various consumer products such as smartwatches and smartphones. Many applications of location-based services have been popularized in these portable devices, driving the need for positioning methods that can achieve meters-level horizontal accuracy without additional computational resources and power consumption (European GNSS Agency, 2018).

Nevertheless, user satisfaction with positioning performance in urban areas remains an issue. A survey of Android users conducted in 2018 by van Diggelen (2021b) underscores this concern, as GNSS performance tends to degrade in cities. This deterioration occurs when buildings and other infrastructure obstruct the line-of-sight (LOS) between the satellite and the receiver. These obstructions may reflect, diffract, or even completely block the satellite signals, causing errors in the measurements and leading to degraded positioning accuracy and reliability. Many studies have attributed multipath interference and non-line-of-sight (NLOS) reception as the main reasons compromising conventional GNSS positioning performance in cities (Groves, 2013; Hsu et al., 2015b; Yuan et al., 2020; Ng et al., 2021).

To alleviate these issues in urban environments, many studies have leveraged 3D building models to provide additional information for navigation and positioning. Those 3D models are often used to predict, at any given location, which satellite signals are directly visible and which are blocked by obstacles, and even in some implementations, to estimate path delays. This information allows GNSS receivers to better interpret and handle the received signals, ultimately enhancing positioning

accuracy and robustness in urban environments. The methods for implementing 3DMA GNSS are flexible and varied. In the past few years, many different 3D-mapping-aided (3DMA) GNSS techniques, e.g., those presented by Suzuki and Kubo (2013); Wang et al. (2015); Suzuki (2016); Hsu et al. (2016); Ziedan (2017, 2019); Groves et al. (2020); Ng et al. (2020); Zhong and Groves (2022a), have been demonstrated to significantly improve the performance of GNSS in cities.

The two primary techniques that underpin 3DMA GNSS positioning are shadow matching and 3DMA ranging. Shadow matching relies on signal strength measurements, comparing them with satellite visibility predictions to evaluate the match of signal behavior to environmental features. The 3DMA ranging, on the other hand, uses pseudo-range measurements, of which NLOS signals are excluded or corrected by 3D models during the calculation. By applying these methods, 3DMA GNSS can provide a more accurate and reliable positioning solution compared to conventional GNSS positioning.

Despite the substantial improvements offered by 3DMA GNSS techniques in urban environments, there remain limitations and challenges that need to be addressed. Taking UCL's 3DMA GNSS algorithms (Zhong and Groves, 2022a,b) as an example, current methodologies struggle to handle scenarios involving overhanging structures. The model used in shadow matching, which relies heavily on signal strength to determine satellite visibility, has to be tuned to the environment to give the best performance. Similarly, in likelihood-based ranging, the pseudo-range error distribution for NLOS signals is described using empirically determined means and variances, which might not capture the complexities involved. Moreover, there is the challenge of ambiguity, where multiple potential solutions may arise in the candidate positions, and taking the average position as the solution is inappropriate. Addressing these limitations is critical for improving the performance and utility of 3DMA GNSS techniques in real-world applications.

The primary purpose of this study is to identify and propose suitable solutions to overcome these limitations. In this light, this study focuses on developing several improvements to the current 3DMA GNSS techniques. These improvements include an enhanced method to predict satellite visibility with overhanging structures, a Bayesian inference-based shadow matching adaptable to different urban environments without re-calibration, a newly designed NLOS model for likelihood-based ranging to provide a more accurate NLOS correction, and a new region growing-based clustering algorithm to handle ambiguity.

The effectiveness of these proposed improvements are validated using GNSS datasets collected in London with a u-blox receiver and a smartphone. The dataset represents a diverse range of urban scenarios, encompassing different building types, heights, and street widths. The aim is to test these improvements under varying conditions to ensure that they can handle the complexity of real-world environments. Both the results of separate tests for each improvement and the results of tests combining all the improvements are analyzed to evaluate their effectiveness in addressing the identified limitations in 3DMA GNSS positioning.

There are many applications that could benefit from this work. Those applications where 3DMA GNSS positioning can be applied could gain performance improvements, such as navigation for pedestrians and vehicles, emergency call location for people and vehicles, navigation for the visually impaired, location-based services, mobile gaming, etc. Other positioning applications that make use of 3D models, such as indoor positioning using Bluetooth, Zigbee, and/or Wi-Fi (Xia et al., 2017), could also gain ideas or inspiration from this work.

This paper has been divided into 5 sections. Section II reviews various 3DMA GNSS positioning methods, and discusses some of the issues using UCL's 3DMA GNSS as an example. Then, in Section III, some improvements, including satellite visibility prediction in semi-open environments, modeling in shadow matching and likelihood-based ranging, and determination of position solution, are explained in detail. Section IV presents the test results of a GNSS dataset collected from multiple test sites in London. The results before and after each improvement are presented separately, followed by the results after applying all the improvements. Finally, the conclusions are summarised in Section V.

II. BACKGROUND

II.1. 3D-Mapping-Aided GNSS

Over the past decade, 3D-mapping-aided (3DMA) GNSS has experienced an upsurge in interest, with its potential to significantly enhance positioning performance in dense urban areas. This improvement is principally achieved through the use of 3D building models, which facilitate predictions about the direct visibility of signals at any given location. Various strategies have been adopted in implementing 3DMA GNSS. These methodologies can broadly be categorized into two types based on their solution determination principles: shadow matching and 3DMA ranging. The former uses the signal strength measurements, while the latter uses the pseudo-ranges. 3DMA GNSS has been implemented in Android fused location provider (van Diggelen, 2021a) and shadow matching is used in the Uber app (Cameron, 2018).

Shadow matching, inspired by the principles of pattern matching, determines the position solution by comparing the received signal strength with the satellite visibility prediction at a series of candidate positions. The concept was independently proposed by Tiberius and Verbree (2004); Saab and Kassas (2006); Ben-Moshe et al. (2011); Groves (2011). Then, Wang et al. (2011, 2015) initially demonstrated the feasibility of the shadow matching technique in cross-street positioning with an accuracy of

several meters. The majority of the research groups working on shadow matching have adopted a hypothesis testing approach, with differences primarily emerging in methods of scoring candidate positions and deriving the overall position solution from candidate position scores. Early research (Wang et al., 2013) relied on a binary value for the measured satellite visibility, obtained through a hard threshold on the signal-to-noise ratio value. The degree of matching between the visibility prediction and measurement used the exclusive not or (XNOR) logical operation that returns true if its inputs are the same, otherwise false. The position solution is finally determined by a weighted average of the coordinates of several candidate points with high scores. Subsequent studies, such as Isaacs et al. (2014); Wang et al. (2015); Wang (2015); Zhang et al. (2020b), advanced the field by introducing probability-based satellite visibility and Bayesian theory-based matching determination, which demonstrated better performance. In contrast to a grid-based approach, Bhamidipati et al. (2022) used constrained zonotopes, a type of convex polytope, to represent buildings and GNSS shadows, enabling propagation of set-valued solutions using vector concatenation operations.

3DMA ranging has been implemented through numerous approaches. One intuitive method involves excluding NLOS signals detected using 3D models from the computation (Obst et al., 2012; Peyraud et al., 2013; Ng and Hsu, 2021). However, this approach necessitates a fairly accurate initial position to enable subsequent NLOS detection algorithms to confidently predict satellite visibility in a timely manner. In urban environments, most positioning applications cannot provide a sufficiently accurate solution within a few seconds after launching. Therefore, these methods are mostly used in continuous positioning.

Instead of simply discarding NLOS measurements, many researchers have sought to use them. One commonly used method is hypothesis testing, where at a series of candidate positions generated around a rough position solution, the path delay of the NLOS signal can be estimated using the 3D building model. These candidate positions are then scored based on the path prediction and the actual measurement (Hsu et al., 2015a, 2016; Gu and Kamijo, 2017; Zhang et al., 2020a). However, these methods often entail high computational demands, particularly for propagation path calculations. Based on the pattern that the pseudo-range error distribution of the LOS signal conforms to a symmetric distribution, while the counterpart of the NLOS signal is asymmetric, Groves et al. (2020) proposed a method known as likelihood-based ranging. This method uses different combinations of error distributions at each candidate position based on the visibility predictions from 3D mapping data, which enables those NLOS pseudo-ranges to participate in the position calculation without explicitly quantifying the additional distance traveled by them.

II.2. UCL's 3DMA GNSS Implementation

UCL's 3DMA GNSS algorithms primarily comprise shadow matching (SM), likelihood-based ranging (LBR), and an integration algorithm, as shown in Figure 1. Both SM and LBR rely on hypothesis testing performed on candidate positions. The candidate positions are defined by a set of three-dimensional coordinates, with the height dimension simplified for land positioning and navigation applications as the sum of terrain height and antenna height above ground.

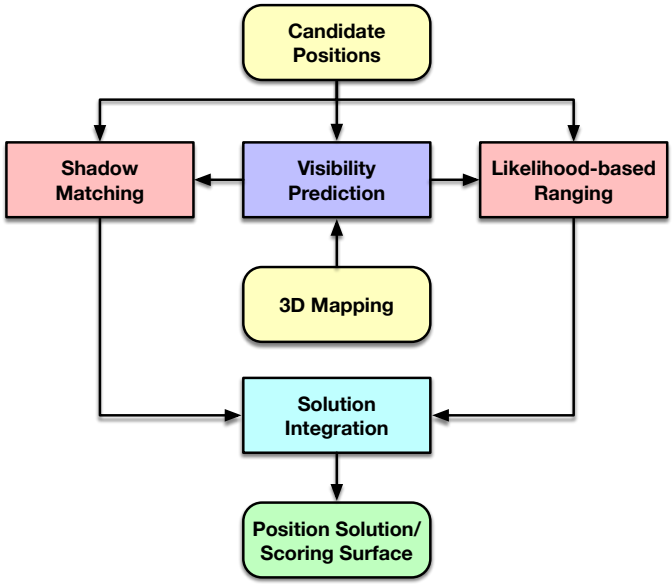

Figure 1: Components of the 3DMA GNSS Core Algorithms

3D mapping data is used to predict the visibility of each satellite signal (i.e., LOS or NLOS) at each candidate position. This

step is relatively computationally intensive and time-consuming. Therefore, an intermediate product, referred to as building boundaries, has been introduced to facilitate real-time operations across a large number of candidate positions. The building boundary specifies the maximum elevation of all buildings within a certain distance at a given azimuth, essentially denoting the minimum elevation for a satellite signal to be directly received in that direction. These boundaries are pre-computed for each candidate position and stored. When required, the signal can be classified as LOS or NLOS by simply comparing the satellite elevation with the building boundary at the corresponding azimuth.

The shadow matching (SM) algorithm (Wang et al., 2015) is designed to determine the position solution by evaluating the degree of matching between actual satellite visibility derived from measured signal strength and predicted visibility at various candidate positions. The algorithm comprises the following steps (Wang et al., 2015; Groves et al., 2020):

1. Determine the predicted visibility of each satellite signal at each candidate position;
2. Determine the measured visibility of each received signal, i.e., the probability being direct LOS, based on the C/N_0 measurement using an appropriate statistical model;
3. Calculate a matching score at each candidate position for each satellite based on its predicted and measured visibility values;
4. Aggregate the matching scores for each satellite at a given candidate position to generate a composite score at that position.

The likelihood-based ranging (LBR) algorithm (Groves et al., 2020) applies different statistical distributions to pseudo-range errors according to satellite visibility predictions, and then evaluates the correspondence between the measured and predicted pseudo-ranges to give the positioning solution. The algorithm comprises the following steps (Groves et al., 2020):

1. Determine the predicted visibility of each satellite signal at each candidate position;
2. Select one of the satellites predicted to be direct LOS as the reference at each candidate position;
3. Calculate the measurement innovation for each satellite at each candidate position by correcting the measured pseudo-range with known errors, such as satellite clock errors, atmospheric delays, and inter-constellation offsets, and then differencing it against the reference satellite to remove receiver clock offset;
4. Determine the cumulative probability of the measurement innovation for each satellite predicted to be NLOS on a skew-normal distribution at each candidate position;
5. Replace these NLOS innovations with corresponding direct LOS innovations possessing the same cumulative probability;
6. Compute the final score for each candidate position using the modified measurement innovations and their corresponding error covariance matrix.

The intention of SM is to improve the accuracy in the direction perpendicular to the street, whereas LBR is considered to be more accurate in the direction along the street. Therefore, a hypothesis-domain integration algorithm (Zhong and Groves, 2022a) is deployed to generate a comprehensive single score for each candidate position based on the scoring surfaces from SM and LBR. The final position solution is thus determined by using the combined scores to weight the candidate positions.

Based on these core algorithms, some extended topics have been explored. Multi-epoch 3DMA GNSS positioning using grid filtering and particle filtering has been found to maximize benefits in mobile positioning in dense environments (Zhong and Groves, 2022a), and 3DMA outlier detection can mitigate to some extent the issues associated with 3D mapping errors and temporary environment changes (Zhong and Groves, 2022b).

II.3. Limitations and Existing Solutions

While the use of 3DMA GNSS has enhanced positioning accuracy and reliability in dense urban environments, certain limitations still exist. These limitations arise from a variety of factors, including the handling of 3D mapping data, neglect of untracked satellites, inadequate modeling of visibility and NLOS signals, and difficulties in managing the ambiguity problem. Some of these limitations are common to all 3DMA GNSS techniques, while others are specific to UCL's implementation.

Accurate prediction of signal visibility is a prerequisite for good 3DMA GNSS performance. One of the limitations stems from the current use of Level of Detail 1 (LoD1) 3D mapping data, which struggles with scenarios that include overhanging structures, such as bridges and balconies. These features are common in urban environments, and they additionally obscure signals from the overhead area compared to the common open-air case, significantly affecting the GNSS signals at high elevation angles. However, most current 3DMA GNSS methods do not fully account for such scenarios, which may cause them to fail in these locations. The use of additional hardware, such as LiDAR and cameras, simplifies the generation of overhead sky plots and facilitates satellite visibility predictions. Some research groups, such as Suzuki and Kubo (2014); Bai et al. (2020); Wen et al. (2021); Wen and Hsu (2022), have demonstrated the use of LiDAR and/or cameras to detect environmental information,

and with slight modifications, these methods can handle the problems posed by overhanging structures. But it is also important to consider the drawbacks associated with these hardware additions, including increased costs and susceptibility to weather conditions, variations in light intensity, and dust accumulation, especially when the sensors are oriented upward.

In dense urban canyon environments, receivers sometimes receive only a limited number of satellite signals, but the ephemeris reveals that the number of satellites overhead is significantly greater than what is actually received, as shown in Figure 2. This is because the direct LOS signals from many satellites are blocked by buildings, and, in some cases, their reflected signals are too weak to be detected by the receiver due to, for example, multiple reflections. The sparse number of signals makes all ranging-based methods challenging, resulting in increased uncertainty in the position solution or even inability to compute the user's position. This is especially true for outlier detection, which typically requires a certain number of measurements to rule out or fix erroneous measurements. However, shadow matching operates differently. Instead of relying on the distance to the satellites, it leverages the visibility of the signals. Therefore, in shadow matching, weak signals that are not detected by the receiver also have the potential to contribute to the positioning solution.

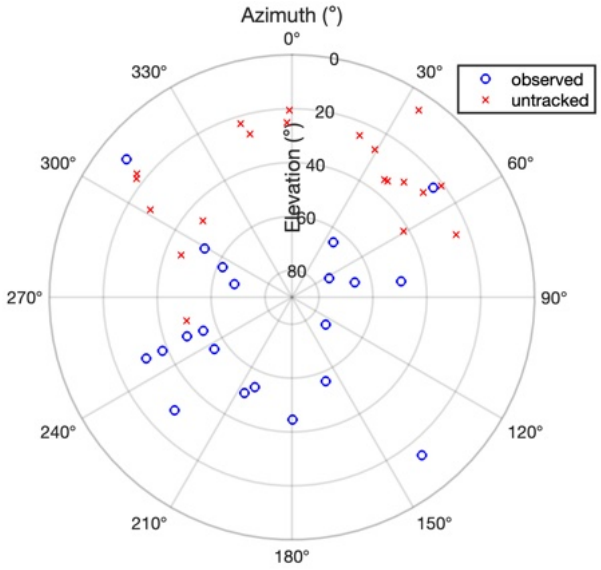

Figure 2: The observed and untracked satellites

Another significant limitation is the inadequacy of the models used in shadow matching and likelihood-based ranging. In conventional shadow matching, satellite visibility determination is solely based on the normalized distribution of signal strength measurements (Wang, 2015). This approach assumes that the number of LOS and NLOS signals are approximately the same in order to obtain better generality. Many subsequent studies, such as Yozevitch et al. (2016); Sun et al. (2019); Xu et al. (2020); Ng et al. (2021), have combined more visibility-related measurements, such as satellite elevation and pseudo-range error, to achieve more accurate LOS/NLOS signal classification, but little attention has been paid to the fact that changes in the environment may alter the prior condition for LOS probability. As shown in Figure 3, the distribution density of buildings varies across different environments. In dense urban areas, NLOS satellites constitute a larger proportion, while in relatively open environments, LOS satellites are more prevalent. Although fine-tuning parameters separately for different environments can yield optimal positioning results, achieving such customization in all areas is impractical, especially considering that urban environments may evolve over time. Conversely, using the same set of parameters may not accurately capture the signal features, such as signal strength distribution, in diverse environments, resulting in inaccurate satellite visibility in particularly dense or open areas.

Similarly, the UCL implementation of likelihood-based ranging may oversimplify the distribution of NLOS path delays by merely relying on an empirically determined set of means and variances. This simplification may result in less accurate NLOS path delay estimations, particularly in environments that significantly differ from the parameter training environment. Therefore, a better model is needed to produce a more accurate correction of NLOS path delay. Several research groups have proposed alternative approaches to accurately estimate NLOS path delays. For instance, Miura et al. (2015); Hsu et al. (2016) employ ray-tracing techniques to calculate NLOS path delays, but require more computational resources and time than likelihood-based ranging. Google then leaves ray-tracing to cloud servers to reduce the computational load on end-users (van Diggelen, 2021a). On the other hand, Ng et al. (2020) uses building boundary and height information to estimate possible reflection points for NLOS reception and calculate path corrections, which is significantly more efficient compared to the

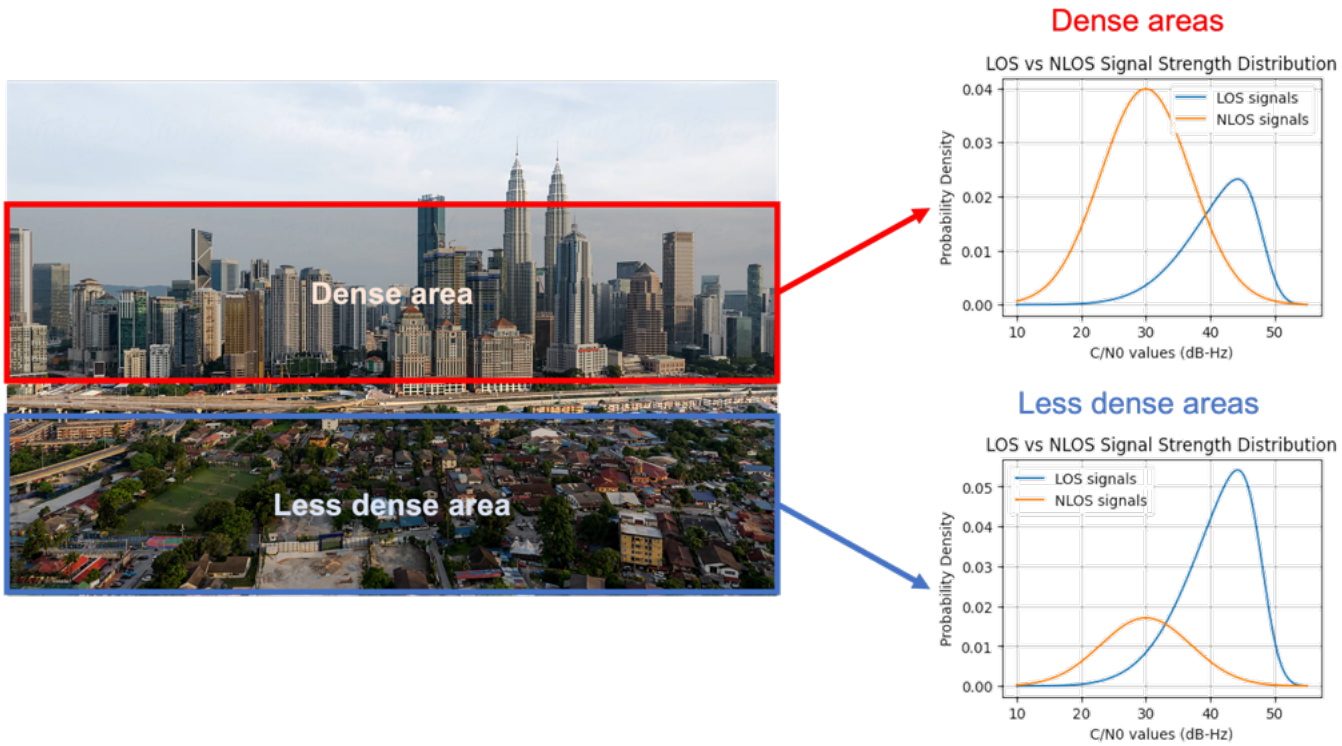

Figure 3: Various densities of buildings and their signal strength distributions

original ray-tracing technique, although still not realizing real-time calculations. Researchers utilizing ray tracing or similar techniques face some challenges that impede their progress. One notable issue is the presence of multiple reflections, which exponentially complicates computations. When multiple potential reflective surfaces are detected, determining the accurate path delay becomes challenging, particularly in scenarios where multiple reflections interact with each other. Balancing accuracy and computational efficiency remains a challenge in estimating NLOS path delays for 3DMA ranging methods.

A further issue arises in the extraction of position solutions from the likelihood surface. As shown in Figure 4, the current approach of weighting candidate locations by their corresponding scores to derive the average position as the solution can potentially pose two problems. Firstly, the solution shifting problem arises when a large cluster of low-scoring candidate positions accumulates, leading to their cumulative scores becoming comparable to those of the high-scoring candidates. Consequently, the position solution can be dragged away from the high-scoring regions towards the low-scoring clusters, causing the solution to deviate from the correct position. Secondly, an ambiguity problem occurs when the search region encompasses more than one potential solution, which is common in densely populated urban areas with closely spaced buildings (Wang et al., 2015). When there are multiple high-scoring regions in the search region, the average solution tends to fall in the centroid of these regions, distancing itself from each individual potential solution. Filtering over multiple epochs is a potential solution to this problem, particularly where a grid or particle filter is used to propagate the likelihood surface across epochs, since it provides a smaller search area and reduces the probability of ambiguity problems (Zhong and Groves, 2022a). However, in single-epoch positioning, the averaged solution treats the entire scoring plane as a single-peaked distribution while introducing a large covariance, which results in a substantial loss of detail in the plane. These remain challenging problems for candidate-based 3DMA GNSS techniques and ones that need to be adequately addressed for better urban positioning.

III. PROPOSED METHODS

III.1. Improved Visibility Determination

The methodology proposed in this research introduces a more robust way of predicting satellite visibility using 3D models, especially in environments with overhanging structures. Previously, visibility predictions were obtained by comparing satellite elevation angles to building boundaries, where the building boundaries are actually the lower elevation constraints for the LOS signal. The new method is formulated based on the same idea.

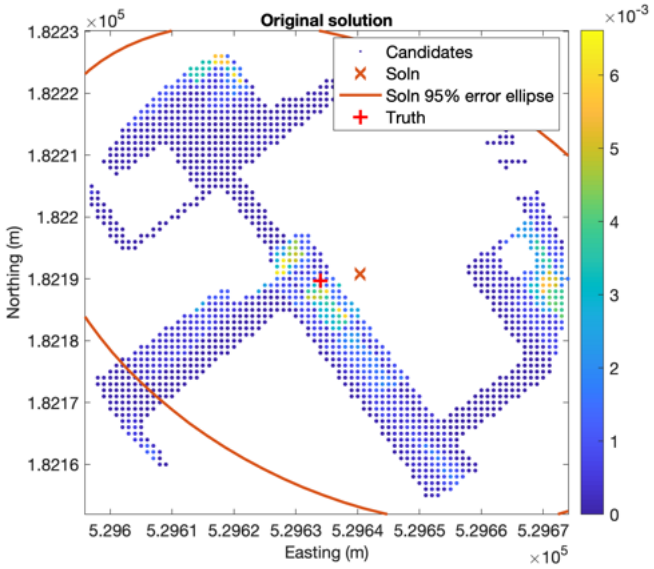

Figure 4: Current method of obtaining solutions from a scoring map

To account for overhanging structures, an upper elevation constraint is introduced. Overhanging structures effectively present a "ceiling" to the sky view, thereby limiting the maximum elevation from which a satellite signal can be received at a given position. This idea helps to delineate the satellite visibility in environments with overhead obstructions and adds a layer of depth to the original prediction model.

Therefore, in the new satellite visibility prediction approach, the measured satellite elevation is compared successively against upper and lower constraints. Satellites below the higher elevation constraint and above the lower elevation constraint are identified as LOS, while the remaining satellites are classified as NLOS.

However, the majority of outdoor locations are overhead unobstructed, meaning that the upper elevation constraint is not frequently applied. This imbalance may lead to computational inefficiency if not addressed properly. To solve this issue, the concept of "feature maps" is introduced. As shown in Figure 5, these maps record the specific features of each candidate location, such as roads, buildings, or tunnels(i.e., overhanging structures). Feature maps streamline the visibility prediction process by providing a reference for the efficient application of elevation constraints. For instance, if a candidate location corresponds to a road feature, the conventional visibility prediction with the lower elevation constraint only is used. However, if a candidate location corresponds to a tunnel feature, where an overhead structure is present, the upper elevation constraint computation is attached to the conventional visibility prediction. Thus, the algorithm is capable of choosing the appropriate visibility prediction scheme based on the feature of the candidate position, promoting flexibility and computational efficiency in the operation.

To enable real-time computation, lower elevation constraints (i.e., building boundaries) at each candidate location are usually pre-computed and stored. Similarly, higher elevation constraints can also be computed in advance. By leveraging feature maps, it becomes possible to store only the higher constraints for candidate points situated in tunnels instead of storing them for all candidate points, which effectively conserves data storage resources while still facilitating efficient processing.

Furthermore, it is crucial to acknowledge that tunnels can present unique scenarios where LOS satellites may be absent, and the likelihood-based ranging may struggle to identify a reference satellite. In such instances, the satellite exhibiting the strongest signal strength is selected as the reference satellite. When the reference satellites are NLOS, some modifications need to be made to the mean and variance of their pseudo-range innovations, as shown in Equations 1 and 2, where the NLOS compensation values are added to the mean and variance of the pseudo-range innovations, respectively.

$$\mu_{ref,NLOS} = \mu_{ref} + \mu_{NLOS,c} \tag{1}$$

$$\sigma^2_{ref,NLOS} = \sigma^2_{ref} + \sigma^2_{NLOS,c} \tag{2}$$

where $\mu_{ref,NLOS}$ and $\sigma^2_{ref,NLOS}$ are the mean and variance of the innovation for NLOS reference satellites, μ_{ref} and σ^2_{ref} are the original mean and variance for the LOS reference satellites, and $\mu_{NLOS,c}$ and $\sigma^2_{NLOS,c}$ are the NLOS compensation values

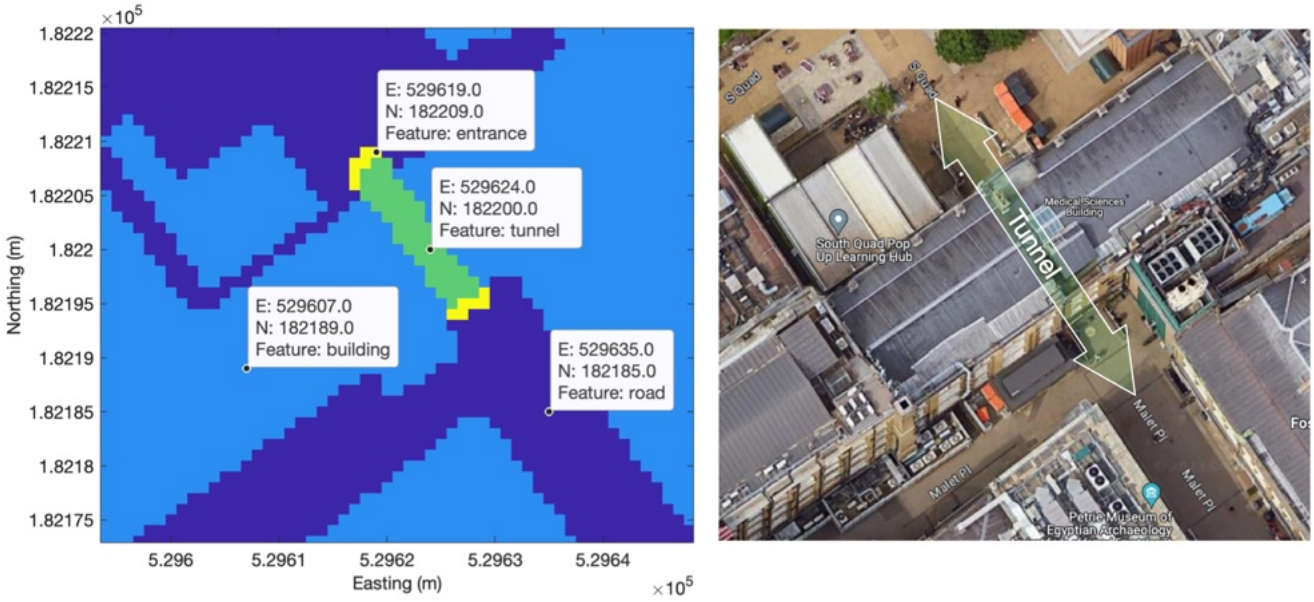

Figure 5: Example of a feature map

for the mean and variance, respectively. This adaptation allows for the continued functionality of likelihood-based ranging even in challenging tunnel environments where LOS satellites are completely unavailable.

III.2. Use of Undetected Signals in Shadow Matching

Undetected signals are those emitted from satellites that are positioned above the receiver's masking angle, but due to obstructions, their signals are not successfully captured by the receiver. Therefore, their measurements, including pseudo-range and signal strength, are not available. Shadow matching requires signal strength measurements and azimuth and elevation angles of the satellite. Consequently, two fundamental problems must be addressed to incorporate undetected signals into the shadow matching process: quantifying the signal strength and determining the satellite's position. These undetected signals predominantly result from weak signal strength, hence, they are directly assigned a nominal value of 0 dB-Hz, which ensures that these untracked signals are always classified as NLOS in subsequent shadow matching. The positions of all healthy satellites in the constellations supported by the receiver are calculated and then checked if they are above the receiver's masking angle. The position of the satellite can be approximated using the ephemeris with an estimated pseudo-range of 2×10^7 meters. Although this estimation may introduce a degree of error, the influence of this error on the calculated azimuth and elevation angles of the satellite is significantly less than 1°. This level of accuracy is generally acceptable for the purposes of shadow matching. By uniformly setting the measured visibility of these undetected signals to NLOS, these weak signals, which would otherwise be ignored, are also able to contribute to the positioning.

III.3. Bayesian Inference-based Shadow Matching

Bayesian Inference, rooted in the principles of Bayesian statistics, provides a mathematical framework for updating probabilities based on new data or evidence. The central pillar of Bayesian inference is Bayes' theorem, which combines prior knowledge and current evidence to generate an updated probability, called a posterior probability. This process can be mathematically expressed using:

$$P(H \mid E) = \frac{P(E \mid H) \cdot P(H)}{P(E)} \tag{3}$$

where $P(H \mid E)$ represents the posterior probability of hypothesis H given evidence E, $P(E \mid H)$ is the likelihood that quantifies the probability of observing evidence E given hypothesis H, $P(H)$ is the prior probability of the hypothesis before considering the evidence, and $P(E)$ is the marginal likelihood, which accounts for the overall probability of observing the evidence across all possible hypotheses being considered.

In the context of shadow matching, the conventional method links the signal strength C/N_0 and the probability of satellite

visibility via a polynomial (Wang, 2015):

$$P(LOS|C/N_0) = \begin{cases} P_{o-\min} & (C/N_0) \leq s_{\min} \\ a_0 + a_1(C/N_0) + a_2[(C/N_0)]^2 & s_{\min} < (C/N_0) < s_{\max} \\ P_{o-\max} & (C/N_0) \geq s_{\max} \end{cases} \tag{4}$$

where $P(LOS|C/N_0)$ is the probability of a signal being LOS given its signal strength, $s_{\min}$ and $s_{\max}$ are the lower and upper bounds of the C/N_0 measurements, and a_0, a_1, a_2 are empirical parameters of the polynomial. This existing approach operates under the assumption of an equal ratio of LOS to NLOS in all environments.

The innovative scheme introduced in this study, as shown in Figure 6, deviates from this assumption, acknowledging that the LOS to NLOS ratio is significantly affected by the environment. For instance, denser urban environments may exhibit a larger share of NLOS signals than LOS signals. Thus, this method assumes that satellites are evenly distributed across the sky, and employs environmental factors to estimate the proportion of LOS and NLOS signals, which is subsequently used as a priori information.

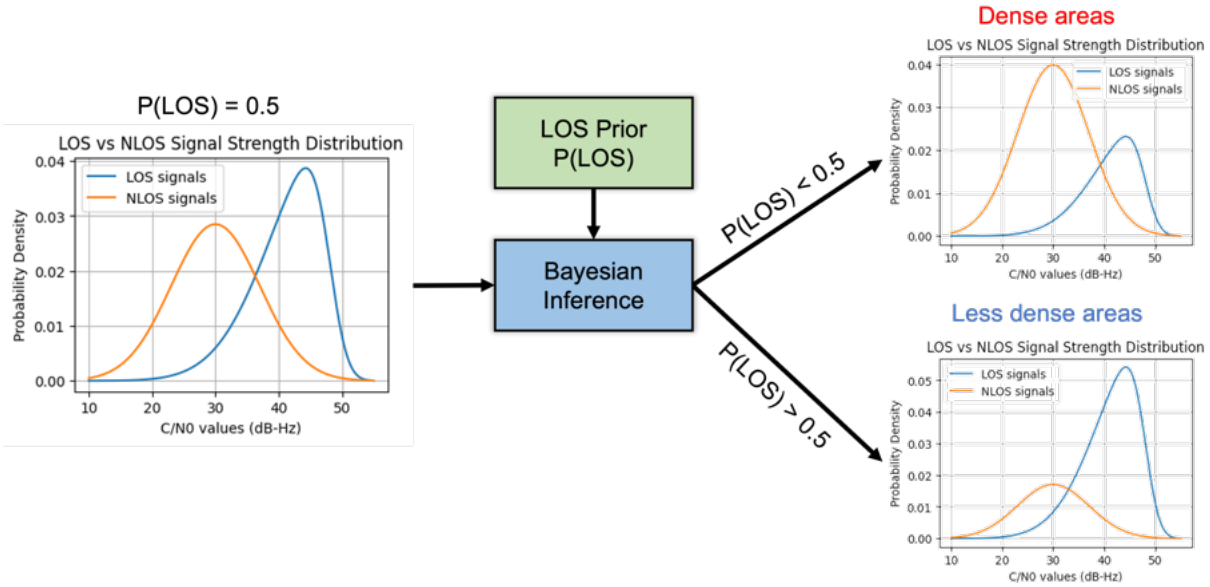

Figure 6: Bayesian inference-based visibility determination

Let $P(LOS)$ be the prior probability. This is the initial assumed probability of a signal being LOS, without considering any specific signal strength. The prior can be effectively derived from the ratio of the number of GNSS signals captured by the receiver to the total number of satellites that are above the receiver masking angle. This ratio provides a rough depiction of the sky occlusion status over the current location of the receiver. A smaller number of captured GNSS signals typically suggests a higher proportion of NLOS signals, indicative of the prevalence of obstructions or interferences in the surrounding environment.

It's also important to consider the azimuth angle. The prior probabilities may be varied in different azimuths. For instance, there should be more LOS satellites in the direction along the street than in the direction across the street. Hence, incorporating azimuth angle into the prior probability calculation offers a refined result. Specifically, when assessing the proportion of captured satellites, only those within a specific range of azimuth angle are considered. This nuanced method, compared to a holistic prior probability, allows for distinctive prior probabilities for signals coming from different directions, thus tailoring the visibility predictions more closely to the actual environment.

Furthermore, it's worth noting that the ability to capture signals can vary due to different antenna and chipset designs. As a result, an empirically determined LOS offset probability has been incorporated into the model to account for these discrepancies. Equation 5 shows the model for the LOS prior probability.

$$P(LOS) = \frac{n_{obs,\alpha\pm\phi}}{n_{obs,\alpha\pm\phi} + n_{untr,\alpha\pm\phi}} + P_{LOS,offset} \tag{5}$$

where $n_{obs,\alpha\pm\phi}$ and $n_{untr,\alpha\pm\phi}$ are the number of captured and untracked satellites within azimuths $\alpha \pm \phi$, respectively, and

$P_{LOS,offset}$ is the LOS offset probability that can be obtained by comparing the proportion of LOS signals in the observed signals to the proportion of signals actually observed from all satellites above the receiver's masking angle.

The value of ϕ can be chosen between 10 and 180 degrees depending on the density of the satellites. The smaller the value of ϕ, the higher the satellite density required, i.e., more satellites are needed to properly compute a prior probability. In the dataset of this paper, there are theoretically about 40 satellites in the sky. Therefore, the value of ϕ was set to 45 degrees to ensure that there are theoretically 10 satellites within the 90-degree azimuth range.

Given the prior probability, the satellite visibility can be calculated using the Bayesian inference formula of Equation 3.

$$P^*(LOS \mid C/N_0) = \frac{P(C/N_0 \mid LOS)P(LOS)}{P(C/N_0)} \tag{6}$$

where $P(C/N_0|LOS)$ is the probability of a LOS signal being identified as LOS for a given C/N_0 value, and $P(C/N_0)$ is the total probability of obtaining the specific signal strength, calculated by the law of total probability:

$$P(C/N_0) = P(C/N_0 \mid LOS)P(LOS) + P(C/N_0 \mid NLOS)P(NLOS) \tag{7}$$

where $P(C/N_0 \mid NLOS) = 1 - P(C/N_0 \mid LOS)$ is the probability of an NLOS signal being defined as LOS at a given signal strength, and $P(NLOS) = 1 - P(LOS)$ is the probability of a signal being NLOS.

Substitute Equation 7 into Equation 6.

$$P^*(LOS \mid C/N_0) = \frac{P(C/N_0 \mid LOS)P(LOS)}{P(C/N_0 \mid LOS)P(LOS) + (1 - P(C/N_0 \mid LOS))(1 - P(LOS))} \tag{8}$$

The value of $P(C/N_0|LOS)$ can be derived from the existing SM satellite visibility model. The current satellite visibility model assumes an equal number of LOS and NLOS signals in the environment, therefore, $P(LOS) = 0.5$ is substituted into Equation 8.

$$P(LOS \mid C/N_0) = \frac{0.5 \times P(C/N_0 \mid LOS)}{0.5 \times P(C/N_0 \mid LOS) + (1 - 0.5) \times (1 - P(C/N_0 \mid LOS))} \tag{9}$$

$$P(LOS \mid C/N_0) = P(C/N_0 \mid LOS) \tag{10}$$

Therefore, the new Bayesian inference-based model can be written by

$$P^*(LOS \mid C/N_0) = \frac{P(LOS \mid C/N_0)P(LOS)}{P(LOS \mid C/N_0)P(LOS) + (1 - P(LOS \mid C/N_0))(1 - P(LOS))} \tag{11}$$

where $P(LOS \mid C/N_0)$ is the normalised satellite visibility model given in Equation 4. At its core, the updated visibility model employs Bayesian inference to weight the signal strength distributions of both LOS and NLOS satellites using the LOS prior probability. This facilitates the model's adaptability across varied environments. The new approach refines satellite visibility by accounting for environmental variables, aligning the algorithm's assumptions more accurately with the specific environment in which it is applied.

III.4. Improved NLOS Modelling in Likelihood-based Ranging

The new NLOS modeling in likelihood-based ranging offers an advanced approach compared to its predecessor. Previously, the distribution of NLOS signal path delay was simply represented by a constant mean and a constant variance. This approach, while functional, could prove oversimplistic when handling complex real-world scenarios. The proposed method instead employs a sophisticated model based on the analysis of signal strength.

Figure 7 shows the mean and variance of the NLOS error as a function of signal strength in the training dataset. The mean value of NLOS error significantly decreases with the increase in signal strength. The core of this new method involves connecting the signal strength with the NLOS path delay. This is achieved by modeling the mean of the path delay μ_{NLOS} with polynomial functions of signal strength measurements, as shown in Equation 12, and keeping the variance σ^2_{NLOS} as a predetermined constant (about $200m^2$ as shown in the right plot of Figure 7).

$$\mu_{NLOS} = b_0 + b_1 \times (C/N_0) \tag{12}$$

where (C/N_0) is the measured signal strength, and b_0 and b_1 are polynomial coefficients determined using the left plot of Figure 7.

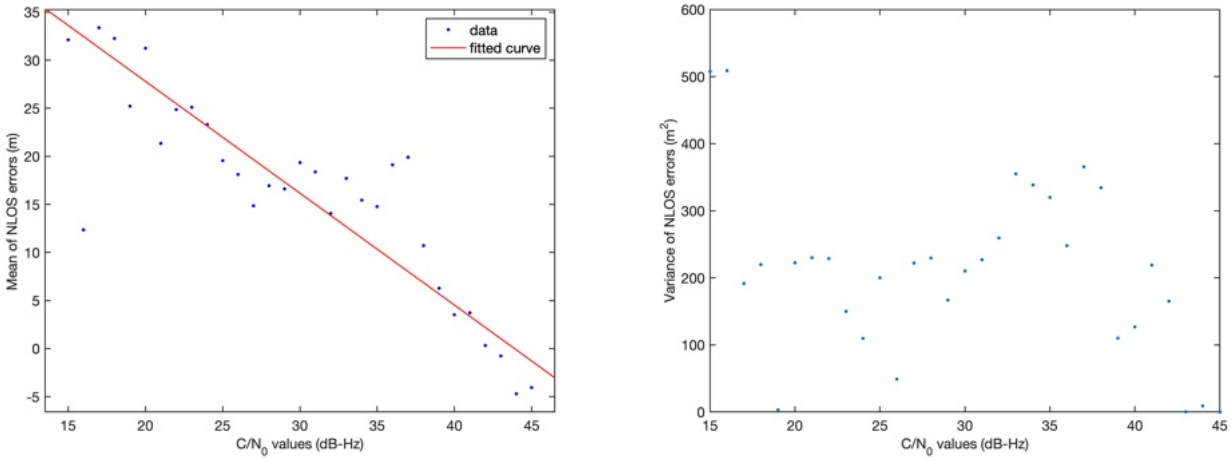

Figure 7: Mean (left plot) and variance (right plot) of NLOS errors (obtained with the training dataset)

III.5. Clustering-based Solution Determination

In the current method of solution extraction, the 3DMA scores weight the candidate positions to obtain an average position. Specifically, normalized 3DMA scores are multiplied by the corresponding position coordinates, and then summed up, as shown in Equation 13.

$$\hat{E} = \frac{\sum_p \Lambda_p E_p}{\sum_p \Lambda_p}$$
$$\hat{N} = \frac{\sum_p \Lambda_p N_p}{\sum_p \Lambda_p} \tag{13}$$

where $\hat{E}$ and $\hat{N}$ are the easting and northing of the solution, Λ_p is the 3DMA score for candidate position p, and E_p and N_p are the easting and northing of candidate position p.

The proposed clustering-based solution determination method, grounded in the region-growing algorithm, addresses issues inherent in the conventional approach of extracting position solutions from likelihood surfaces, specifically those related to solution shifting and ambiguity.

To resolve the problem of shifting caused by the aggregation of a large number of low-scoring points, candidate positions are first ranked in descending order of their scores. Then, the cumulative sum of the scores is calculated, and a threshold is set to filter out low-scoring candidates. The threshold is set to 0.68, representing one standard deviation of the normal distribution. Low-scoring candidates are removed sequentially, from the lowest to higher scores, until the cumulative score of the remaining candidates falls below this threshold. This reduction of low-scoring candidates diminishes their impact on the final solution and decreases the possibility of occurrence of solution shifting, allowing the algorithm to focus on areas with higher likelihoods when determining position solutions.

For mitigating the ambiguity issue, where likelihood surfaces may contain multiple high-scoring regions (as shown in Figure 4), clustering or segmentation methods need to be used. These allow for the segmentation of different high-scoring regions, thus enabling 3DMA GNSS to provide multiple location solutions rather than a single averaged solution. In addition, the new algorithm needs to possess the capability to automatically determine the number of potential solutions, since the number of high-scoring regions is unknown.

The region-growing algorithm is a simple and efficient technique in image processing (Adams and Bischof, 1994) that aims to group pixels or regions in an image based on their similarity. This algorithm starts with an initial seed pixel or region and iteratively expands the region by incorporating neighboring pixels that satisfy certain criteria, such as similarity in color, intensity, and texture.

In the context of extracting position solutions from 3DMA scoring surfaces, the score of each candidate becomes the basis for the similarity criterion. The selection of seed candidates is critical to the algorithm's success. A threshold related to the cumulative sum of the scores is established, and candidates with scores higher than this threshold are considered as seeds. With the removal of low-scoring candidates in the earlier stage, the proposed algorithm simplifies the region-growing process

by starting with a seed candidate and iteratively expanding the region through the addition of neighboring candidates until no additional candidates can be incorporated. The result is a region or a set of regions consisting of only high-scoring candidates. Finally, a weighted position solution is computed for each region.

It is worth noting that there are two special cases that may occur during the region-growing process. First, high-scoring candidates surrounded by low-scoring ones should be regarded as outliers since neighboring candidates are expected to exhibit similar satellite visibility characteristics. Second, regions that are not reached by the algorithm due to the absence of high-scoring seed candidates should also be deemed outliers. This is because other regions might provide superior solutions, implying that these untouched candidates do not contribute optimal results.

After obtaining several regional candidate solutions, a selection algorithm is needed to pick one of them as the final positioning solution. In this paper, since no other information is available, the candidate solutions are compared with the conventional GNSS position solution, and the one with the smallest Mahalanobis distance from the conventional solution will be selected as the final solution.

IV. EXPERIMENTS

IV.1. Experimental Setup

The dataset used for testing in this study was collected in May and July of 2023 within the main campus of University College London (UCL). This dataset captures GNSS signals from various constellations, including GPS, GLONASS, Galileo, and Beidou, using a u-blox ZED-F9P GNSS receiver. Figure 8 illustrates the 9 experimental sites, with 4 sites (labeled in orange) located in tunnels and the remaining 5 sites (labeled in blue) situated outdoors. These locations were selected to represent diverse scenarios and conditions for a comprehensive evaluation of the proposed algorithms. Each segment consists of a 3-minute GNSS observation, with a recording frequency of 1 Hz. During the collection, the antenna was consistently held at a height of 1.2 meters above the ground. For ground truth, the relative distances from the antenna to the proximate landmarks were measured via a laser rangefinder, and the true position coordinates were later extracted from the Ordnance Survey MasterMap, denoted as easting and northing projected coordinates on the OSGB36 datum.

Figure 8: Testing sites (Background map ©Google Maps)

For a more detailed understanding of the data characteristics from each location, Table 1 summarizes essential attributes of the dataset, which provides the number of epochs per segment, the true position expressed in projected coordinates on the OSGB36

datum, and the observational statistics. These statistics include the average number of satellites observed per epoch $\bar{n}_{sat}$, the average number of NLOS signals per epoch $\bar{n}_{NLOS}$ (determined by the 3D mapping data at the true positions), the mean and standard deviation of the C/N_0, represented as μ_{C/N_0} and σ_{C/N_0}, respectively, and the mean and standard deviation of the elevation, represented as μ_{elev} and σ_{elev}, respectively.

Table 1: Experimental information

ID	No. of epochs	True position coordinates, m (Easting, Northing)	$\bar{n}_{sat}$	$\bar{n}_{NLOS}$	μ_{C/N_0}, dB-Hz	σ_{C/N_0}, dB-Hz	μ_{elev}, degrees	σ_{elev}, degrees
T1	180	(529620.10, 182206.84)	11.9	11.9	29.5	8.2	40.4	19.3
T2	180	(529626.05, 182197.09)	9.1	8.1	25.0	8.3	40.1	18.8
T3	180	(529660.15, 182290.55)	16.5	16.5	26.2	7.2	42.5	22.1
T4	180	(529668.88, 182295.96)	21.2	20.5	28.4	6.1	38.4	21.1
R1	180	(529564.01, 182156.94)	26.9	12.8	34.0	9.3	40.1	22.9
R2	180	(529633.99, 182189.71)	24.8	17.9	33.9	7.6	44.5	20.1
R3	180	(529648.58, 182163.83)	24.8	19.3	29.9	9.6	43.5	19.8
R4	180	(529655.05, 182280.84)	21.3	17.8	33.2	8.5	47.4	18.7
R5	180	(529690.73, 182297.49)	31.0	13.6	36.2	8.3	39.2	20.5

Furthermore, for the purpose of algorithm parameter tuning, a distinct training dataset was employed. This training data, acquired in 2022 in London using the same receiver, provides a comprehensive yet independent base for tuning. In addition, it does not include any locations in tunnels.

IV.2. Experimental Results

Each enhancement was verified and tested individually, followed by the results of the 3DMA GNSS algorithm that combines all the enhancements. The impact of some enhancements might not be readily discernible from the RMS errors in position solutions. Therefore, to better present the overall effect of each enhancement on 3DMA scoring, the scoring maps from all epochs at every test site were averaged to produce average scoring maps. Detailed average scoring maps for each enhancement can be found in Appendix B. For testing convenience and visualization purposes, during the validation of each enhancement, the search area for the 3DMA algorithm was standardized to a circular region with a 40-meter radius, centered around the true position. However, in the final showcased results, the 3DMA search area is a dynamic elliptical area, centered around the conventional GNSS position solution and shaped in accordance with its covariance (at 99% confidence). Therefore, it is important to recognize that the scoring charts in Appendix B are not directly correlated with the positioning results in Figure 10 and Appendix A.

Figures 11, 12, and 13 in Appendix B respectively show the test results of Shadow matching (SM), likelihood-based ranging (LBR), and their integration without the support for tunnels or any other enhancements. The previous version of the 3DMA algorithm fails to obtain correct position solutions in all tunnel tests, while proper results are obtained in regular outdoor tests, except for Site R2. In Site R2, SM performs well, while LBR is the main reason for the poor performance. This may be due to the fact that the pseudo-range innovation distribution at Site R2 does not fit well with the pre-determined model. With the introduction of tunneling support, the 3DMA GNSS algorithm is able to successfully operate within tunnels as shown in Sites T1-T4 in Figures 14, 15, and 16. In tunnel environments, SM demonstrates strong performance, accurately providing position solutions. In contrast, LBR struggles in tunnels due to the lack of direct LOS satellites, as evidenced by Sites T1-T4 in Table 1. The absence of LOS signals causes LBR to pick only NLOS satellites as the reference, introducing additional errors. Unlike ray-tracing techniques, our version of LBR does not explicitly compute NLOS errors, so in tunnel scenarios, all the pseudo-range innovations need to be remapped from the asymmetric to the symmetric distributions, which poses a significant challenge to the accuracy of LBR.

Given that the original 3DMA GNSS algorithm struggles with tunnel scenarios and adding tunnel support does not significantly change the original scoring maps in regular outdoor sites, all subsequent comparisons will be drawn between the original 3DMA GNSS with tunnel support and the enhanced 3DMA GNSS which integrates any additional enhancements.

As shown in Figure 2, in urban environments, a significant number of satellite signals are not tracked by the receiver due to blockage. The performance of SM can be improved after considering all GNSS signals including the untracked ones. As shown in Figure 14 in Appendix B, there are multiple relatively high-scoring regions in the scoring map due to the small number of

satellites observed. After complementing all possible satellites in the sky, as shown in Figure 17 in Appendix B, the performance of SM is enhanced at most of the test sites. It can be seen from Figure 17 that the ambiguity problem is improved and the high-scoring areas near the true position become more obvious compared to Figure 14. Combined with the example sky map shown in Figure 2, it can be found that the involvement of untracked satellites can improve the satellite geometric distribution, allowing the determination of some NLOS regions obscured by buildings to be supported by measurement data. However, it is worth noting that at some of the test sites, such as T4 and R5, the results became worse with the inclusion of untracked satellites compared to the original results, since some of the untracked signals were incorrectly classified as NLOS. This is unavoidable because signal strength measurements are missing for these untracked satellites and the vast majority of them are NLOS.

Compared to the results presented in Figure 17, the outcomes in Figure 18 in Appendix B not only incorporate untracked signals but also employ Bayesian inference to integrate the LOS prior probability. The results demonstrate that after applying Bayesian inference, some erroneous high-scoring regions have disappeared (as seen in Sites R2 and R4), which further alleviates the ambiguity issues frequently observed in SM. However, it appears that Bayesian inference can offer only refinements to the results of SM, and struggles to substantially shift the high-scoring regions or to correct the solutions.

Figure 19 in Appendix B shows the average scoring maps of the enhanced LBR. Compared to the results shown in Figure 15, the enhanced LBR does not exhibit significant changes in the scoring maps, and its performance improved at some sites, such as Sites T2 and T4, while it slightly deteriorated at Sites R3 and R5. Among all test points, the most notable effect of the enhanced LBR appears at Site T3, where it illuminates the area surrounding the true position. For Site R2, where the original LBR was ineffective, the new NLOS error model did not bring a fundamental improvement. This is attributed to the fact that the pseudo-range innovation distribution at R2 does not align well with the predefined model, and the fine-tuning of the NLOS error model shown in Figure 7 cannot fundamentally change their match.

Figure 20 shows the integrated results of enhanced SM and LBR. The combination of the enhanced SM and LBR makes the positioning solution better, and the integrated solution is significantly better than the individual solutions of SM or LBR at most test sites. Compared with the original 3DMA results shown in Figure 16, the enhanced 3DMA GNSS algorithm primarily exhibits improvements in positioning results within tunnel environments.

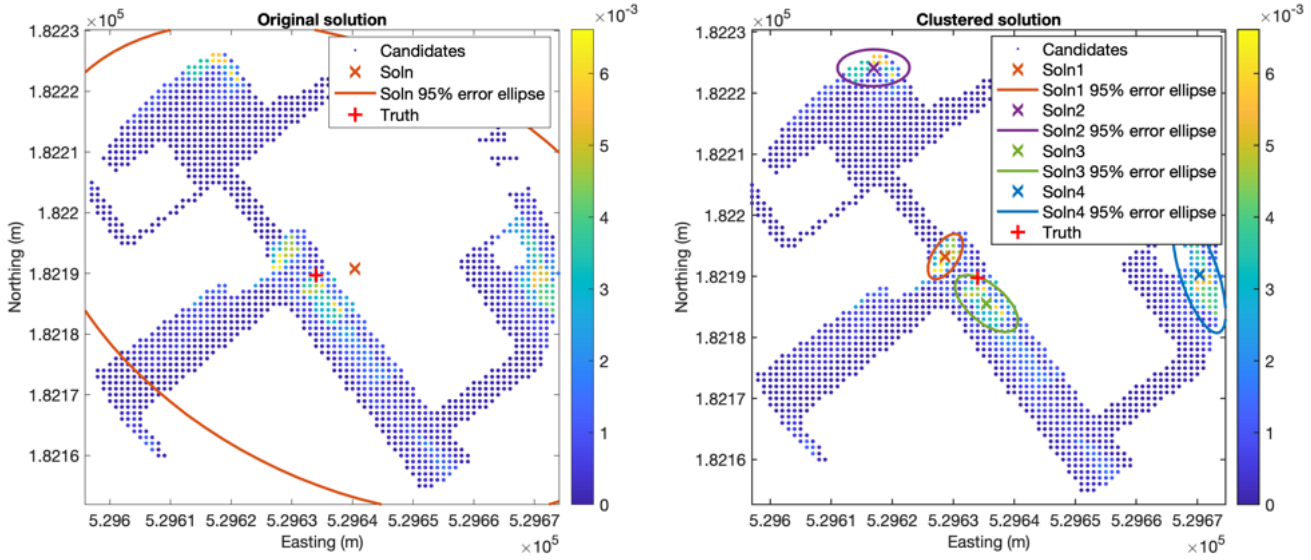

Figure 9: Example of original (left plot) and regional (right plot) position solutions at Site R2 (using enhanced SM that incorporates support for tunnels and fusion of untracked satellites)

Figure 9 shows the effect of clustering. In the original scheme, the position solution is located in the middle of several high-scoring regions but does not belong to any of them. The clustering algorithm is able to provide multiple position solutions, each of which is an optimal solution in the high-scoring region it belongs to. Therefore, it is required to select one of these candidate position solutions as the final solution. It is important to note that the clustering algorithm is not guaranteed to give an optimal solution, it only provides multiple candidates for position solutions. Subsequent selection algorithms, combined with other information, such as the conventional ranging solutions, are then tasked to choose one as the final solution. If an incorrect candidate solution is selected, such as Solution 2 in the right plot of Figure 9, the resulting solution can be inferior compared to the averaged solution presented in the left plot of Figure 9. In summary, the clustering algorithm achieves its best

performance when multiple high-scoring regions appear on the scoring map, and the selection algorithm successfully filters out robust candidate position solutions.

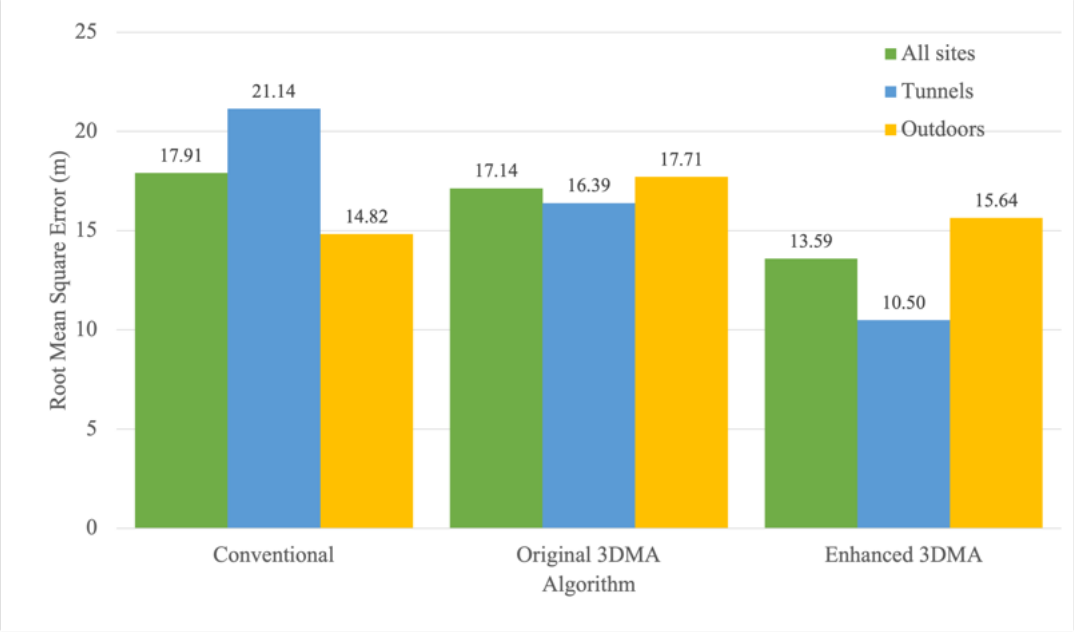

Figure 10: Horizontal radial position root mean square (RMS) error

After each of the enhancements was validated, they were all applied to the original 3DMA GNSS algorithm. In Figure 10, the bars show, from left to right, the results of the conventional GNSS, the original 3DMA GNSS with tunnel support, and the enhanced 3DMA GNSS, and the detailed results can be found in Appendix A. Based on the statistical data shown in Figure 10, the enhanced 3DMA GNSS algorithm improves the RMS position error in the horizontal radial direction by more than 20% compared to the original one. From the detailed data in Appendix A, it is evident that a significant portion of the errors can be attributed to the positioning results at Site R2. In simpler terms, the 3DMA GNSS fails to provide an accurate position solution at Site R2. Upon reviewing the scoring plots in Appendix B, it becomes apparent that while SM performs reasonably well at Site R2, both the original and enhanced LBR consistently fail to offer satisfactory results, becoming the primary reason for the integrated solution deviating from the true position. After excluding the results from Site R2, the original and enhanced 3DMA GNSS algorithms yielded horizontal position RMS errors of 11.9m and 8.2m, respectively. In other words, the enhanced 3DMA GNSS shows an improvement of approximately 31% in horizontal positioning accuracy over the original algorithm. In addition, as can be seen in Table 2, the enhanced 3DMA GNSS provides a greater improvement in tunnel environments than in regular sites. This might be attributed to the fact that on regular locations other than R2, the original 3DMA GNSS is already capable of achieving an accuracy of around 5 meters of RMS position error, which may have made it difficult to further improve the performance with these small enhancements.

V. CONCLUSIONS

In urban environments, multipath interference and NLOS reception are still the main constraints on GNSS performance. Although 3DMA GNSS has been shown to improve positioning performance in urban areas, there are still a number of issues that need to be addressed.

This paper introduced a series of targeted improvements to the existing UCL 3DMA GNSS algorithm. Notably, these improvements encompass support for tunnels, incorporation of untracked satellites in shadow matching, integration of prior probabilities through Bayesian inference in shadow matching, refinement of the NLOS error model in likelihood-based ranging, and the provision for multiple regional position solutions. Each of these improvements was validated and tested on a practically collected dataset.

The experimental results show that by improving 3DMA GNSS in various aspects, its positioning performance in urban environments can be improved. Specifically, compared to the original algorithm, the enhanced 3DMA GNSS reduces the horizontal position RMS error in single epoch positioning by about 20%. After excluding the results from Site R2, where the 3DMA GNSS failed, the horizontal RMS errors produced by the original and enhanced 3DMA GNSS algorithms are 11.9m

and 8.2m, respectively, and the enhanced 3DMA GNSS shows an improvement of approximately 31% compared to the original algorithm.

VI. FUTURE WORK

The current version of the 3DMA GNSS positioning algorithm still has some room for improvement. Areas worth exploring further include:

- Kinematic positioning test.

  In this paper, the effectiveness of the proposed methods has been tested in static positioning, whereas in reality pedestrians and vehicles are usually in motion. Therefore, these algorithms need further proof of their effectiveness in tests with pedestrians and vehicles in motion.

- Selection algorithm for regional solutions.

  While the region-growing algorithm provides multiple position solution candidates, this still requires a robust selection algorithm to pick the final solution. With more information, it might be possible to accurately select the solution that is closest to the true position.

ACKNOWLEDGEMENTS

Qiming Zhong is funded by the China Scholarship Council and a UCL Engineering Faculty Scholarship.

REFERENCES

Adams, R. and Bischof, L. (1994). Seeded region growing. *IEEE Transactions on Pattern Analysis and Machine Intelligence*, 16:641–647.

Bai, X., Wen, W., and Hsu, L. (2020). Using Sky-pointing fish-eye camera and LiDAR to aid GNSS single-point positioning in urban canyons. *IET Intelligent Transport Systems*, 14:908–914.

Ben-Moshe, B., Elkin, E., Levi, H., and Weissman, A. (2011). Improving accuracy of GNSS devices in urban canyons. *Proceedings of the 23rd Annual Canadian Conference on Computational Geometry, CCCG 2011*.

Bhamidipati, S., Kousik, S., and Gao, G. (2022). Set-Valued Shadow Matching Using Zonotopes for 3D-Map-Aided GNSS Localization. *NAVIGATION: Journal of the Institute of Navigation*, 69:navi.547.

Cameron, A. (2018). PNT Roundup: Uber turns on shadow matching. *GPS World*, page 12. `https://www.gpsworld.com/pnt-roundup-uber-turns-on-shadow-matching/`.

European GNSS Agency (2018). *GNSS user technology report. Issue 2*. Publications Office of the European Union. `https://data.europa.eu/doi/10.2878/743965`.

Groves, P. D. (2011). Shadow matching: A new GNSS positioning technique for urban canyons. *Journal of Navigation*, 64(3):417–430.

Groves, P. D. (2013). *Principles of GNSS, inertial, and multisensor integrated navigation systems*. Artech House, Boston; London.

Groves, P. D., Zhong, Q., Faragher, R., and Esteves, P. (2020). Combining inertially-aided extended coherent integration (Supercorrelation) with 3D-mapping-aided GNSS. In *Proceedings of the 33rd International Technical Meeting of the Satellite Division of the Institute of Navigation, ION GNSS+ 2020*, pages 2327–2346. Institute of Navigation (ION).

Gu, Y. and Kamijo, S. (2017). GNSS positioning in deep urban city with 3D map and double reflection. In *2017 European Navigation Conference, ENC 2017*, pages 84–90. Institute of Electrical and Electronics Engineers Inc.

Hsu, L. T., Gu, Y., and Kamijo, S. (2015a). NLOS correction/exclusion for GNSS measurement using RAIM and city building models. *Sensors (Switzerland)*, 15(7):17329–17349.

Hsu, L. T., Gu, Y., and Kamijo, S. (2016). 3D building model-based pedestrian positioning method using GPS/GLONASS/QZSS and its reliability calculation. *GPS Solutions*, 20(3):413–428.

Hsu, L. T., Jan, S. S., Groves, P. D., and Kubo, N. (2015b). Multipath mitigation and NLOS detection using vector tracking in urban environments. *GPS Solutions*, 19(2):249–262.

Isaacs, J. T., Irish, A. T., Quitin, F., Madhow, U., and Hespanha, J. P. (2014). Bayesian localization and mapping using GNSS SNR measurements. In *Record - IEEE PLANS, Position Location and Navigation Symposium*, pages 445–451.

Miura, S., Hsu, L. T., Chen, F., and Kamijo, S. (2015). GPS Error Correction With Pseudorange Evaluation Using Three-Dimensional Maps. *IEEE Transactions on Intelligent Transportation Systems*, 16:3104–3115.

Ng, H. F. and Hsu, L. T. (2021). 3D Mapping Database Aided GNSS RTK and Its Assessments in Urban Canyons. *IEEE Transactions on Aerospace and Electronic Systems*.

Ng, H. F., Zhang, G., and Hsu, L. T. (2020). A Computation Effective Range-Based 3D Mapping Aided GNSS with NLOS Correction Method. *Journal of Navigation*, 73(6):1202–1222.

Ng, H. F., Zhang, G., and Hsu, L. T. (2021). Robust GNSS Shadow Matching for Smartphones in Urban Canyons. *IEEE Sensors Journal*, 21(16):18307–18317.

Obst, M., Bauer, S., and Wanielik, G. (2012). Urban multipath detection and mitigation with dynamic 3D maps for reliable land vehicle localization. In *Record - IEEE PLANS, Position Location and Navigation Symposium*, pages 685–691.

Peyraud, S., Bètaille, D., Renault, S., Ortiz, M., Mougel, F., Meizel, D., and Peyret, F. (2013). About non-line-of-sight satellite detection and exclusion in a 3D map-aided localization algorithm. *Sensors (Switzerland)*, 13(1):829–847.

Saab, S. S. and Kassas, Z. M. (2006). Power matching approach for GPS coverage extension. *IEEE Transactions on Intelligent Transportation Systems*, 7(2):156–166.

Sun, R., Hsu, L.-T., Xue, D., Zhang, G., and Ochieng, W. Y. (2019). GPS Signal Reception Classification Using Adaptive Neuro-Fuzzy Inference System. *Journal of Navigation*, 72:685–701.

Suzuki, T. (2016). Integration of GNSS positioning and 3D map using particle filter. *29th International Technical Meeting of the Satellite Division of the Institute of Navigation, ION GNSS 2016*, 2:1296–1304.

Suzuki, T. and Kubo, N. (2013). Correcting GNSS multipath errors using a 3D surface model and particle filter. *26th International Technical Meeting of the Satellite Division of the Institute of Navigation, ION GNSS 2013*, 2:1583–1595.

Suzuki, T. and Kubo, N. (2014). N-LOS GNSS Signal Detection Using Fish-Eye Camera for Vehicle Navigation in Urban Environments. In *Proceedings of the 27th International Technical Meeting of the Satellite Division of The Institute of Navigation (ION GNSS+ 2014)*, pages 1897–1906.

Tiberius, C. and Verbree, E. (2004). GNSS positioning accuracy and availability within Location Based Services: The advantages of combined GPS-Galileo positioning. In *NaviTec*.

van Diggelen, F. (2021a). End Game for Urban GNSS: Google's Use of 3D Building Models. *Inside GNSS*. `https://insidegnss.com/end-game-for-urban-gnss-googles-use-of-3d-building-models/`.

van Diggelen, F. (2021b). Google's Use of 3D Building Models to Solve Urban GNSS. `https://www.ion.org/itm/abstracts.cfm?paperID=10048`.

Wang, L. (2015). *Investigation of Shadow Matching for GNSS Positioning in Urban Canyons*. PhD thesis, University College London.

Wang, L., Groves, P. D., and Ziebart, M. K. (2011). GNSS Shadow Matching Using A 3D Model of London. In *European Navigation Conference*.

Wang, L., Groves, P. D., and Ziebart, M. K. (2013). Urban positioning on a smartphone: Real-time shadow matching using GNSS and 3D City Models. *26th International Technical Meeting of the Satellite Division of the Institute of Navigation, ION GNSS 2013*, 2:1606–1619.

Wang, L., Groves, P. D., and Ziebart, M. K. (2015). Smartphone shadow matching for better cross-street GNSS positioning in urban environments. *Journal of Navigation*, 68(3):411–433.

Wen, W. and Hsu, L. T. (2022). 3D LiDAR Aided GNSS NLOS Mitigation in Urban Canyons. *IEEE Transactions on Intelligent Transportation Systems*, 23:18224–18236.

Wen, W., Zhang, G., and Hsu, L. T. (2021). GNSS NLOS Exclusion Based on Dynamic Object Detection Using LiDAR Point Cloud. *IEEE Transactions on Intelligent Transportation Systems*, 22:853–862.

Xia, S., Liu, Y., Yuan, G., Zhu, M., and Wang, Z. (2017). Indoor fingerprint positioning based on Wi-Fi: An overview. *ISPRS International Journal of Geo-Information*, 6:135.

Xu, H., Angrisano, A., Gaglione, S., and Hsu, L.-T. (2020). Machine learning based LOS/NLOS classifier and robust estimator for GNSS shadow matching. *Satellite Navigation*, 1:15.

Yozevitch, R., Moshe, B. B., and Weissman, A. (2016). A Robust GNSS LOS/NLOS Signal Classifier. *NAVIGATION*, 63:429–442.

Yuan, Y., Shen, F., and Li, X. (2020). GPS multipath and NLOS mitigation for relative positioning in urban environments. *Aerospace Science and Technology*, 107:106315.

Zhang, G., Ng, H.-F., Wen, W., and Hsu, L. T. (2020a). 3D Mapping Database Aided GNSS Based Collaborative Positioning Using Factor Graph Optimization. *IEEE Transactions on Intelligent Transportation Systems*, pages 1–13.

Zhang, G., Wen, W., Xu, B., and Hsu, L. T. (2020b). Extending Shadow Matching to Tightly-Coupled GNSS/INS Integration System. *IEEE Transactions on Vehicular Technology*, 69(5):4979–4991.

Zhong, Q. and Groves, P. D. (2022a). Multi-Epoch 3D-Mapping-Aided Positioning using Bayesian Filtering Techniques. *NAVIGATION: Journal of the Institute of Navigation*, 69(2).

Zhong, Q. and Groves, P. D. (2022b). Outlier Detection for 3D-Mapping-Aided GNSS Positioning. *Proceedings of the 35th International Technical Meeting of the Satellite Division of The Institute of Navigation (ION GNSS+ 2022)*, pages 2104–2126.

Ziedan, N. I. (2017). Urban positioning accuracy enhancement utilizing 3D buildings model and accelerated ray tracing algorithm. *30th International Technical Meeting of the Satellite Division of the Institute of Navigation, ION GNSS 2017*, 5:3253–3268.

Ziedan, N. I. (2019). Enhancing GNSS mobile positioning in urban environments through utilization of multipath prediction and consistency analysis. *Proceedings of the 32nd International Technical Meeting of the Satellite Division of the Institute of Navigation, ION GNSS+ 2019*, pages 3469–3483.

APPENDIX A DETAILED EXPERIMENTAL RESULTS

Table 2: Horizontal radial position RMS errors (in metres) for different algorithms

Site ID	Conventional GNSS	Original 3DMA (with tunnel support)	Enhanced 3DMA
T1	24.74	17.90	9.74
T2	16.34	19.35	12.12
T3	18.32	17.04	13.55
T4	23.94	9.49	3.89
T1-T4	21.14	16.39	10.50
R1	15.40	3.81	3.67
R2	26.15	38.84	33.56
R3	5.26	5.17	6.76
R4	10.32	3.04	4.75
R5	6.62	3.02	3.83
R1-R5	14.82	17.71	15.64
Overall	17.91	17.14	13.59

Table 3: Horizontal radial position errors (in metres) for different algorithms, 90% of confidence

Site ID	Conventional GNSS	Original 3DMA (with tunnel support)	Enhanced 3DMA
T1	28.38	20.81	14.30
T2	28.85	29.14	24.93
T3	27.40	27.65	25.66
T4	27.99	12.17	2.56
T1-T4	28.26	24.18	19.61
R1	19.56	5.49	4.71
R2	31.95	42.63	41.81
R3	7.56	8.02	8.84
R4	12.86	3.70	5.20
R5	10.35	1.57	3.09
R1-R5	27.08	39.82	40.96
Overall	27.73	35.33	25.53

Table 4: Horizontal radial position errors (in metres) for different algorithms, 50% of confidence

Site ID	Conventional GNSS	Original 3DMA (with tunnel support)	Enhanced 3DMA
T1	25.23	17.57	1.45
T2	11.15	16.39	1.48
T3	17.55	13.31	2.51
T4	23.29	8.87	1.54
T1-T4	20.65	14.62	1.56
R1	15.05	3.46	3.09
R2	27.08	39.82	40.97
R3	4.80	4.48	5.99
R4	10.12	2.82	4.56
R5	6.32	1.09	1.85
R1-R5	10.05	3.31	4.45
Overall	14.12	7.36	3.18

APPENDIX B DETAILED DEMONSTRATION OF EACH ENHANCEMENT

To demonstrate the actual effect of each small enhancement, Figures 11 through 20 show the average scoring maps over 180 seconds at each test site. A fixed search area, i.e., a circular area with a radius of 40 meters centered on the true position, was used for ease of computation. The points in the figure indicate candidate positions. The color of these points denotes their likelihood, with brighter color symbolizing a higher probability of being the positioning solution. Any blank spaces represent either indoor areas or areas outside the search range.

Figures 11, 12, and 13 depict the scoring surfaces for the original shadow matching (SM), likelihood-based ranging (LBR), and integrated results. Introducing tunnel environment support modifies the scoring surfaces as demonstrated in Figures 14, 15, and 16.

Other enhanced capabilities are then introduced on top of the tunnel support. Figure 17 shows the SM results incorporating untracked satellites. Figure 18 takes this SM algorithm a step further, showing the inclusion of untracked satellites and the fusion of visibility priors with Bayesian inference. Figure 19 presents an enhanced LBR scoring surface with a more sophisticated NLOS path delay model. Lastly, Figure 20 integrates the results from both the enhanced SM and LBR.

Note that these plots only visualize the effect of each enhancement and do not represent the results associated with Figure 10 and Appendix A.

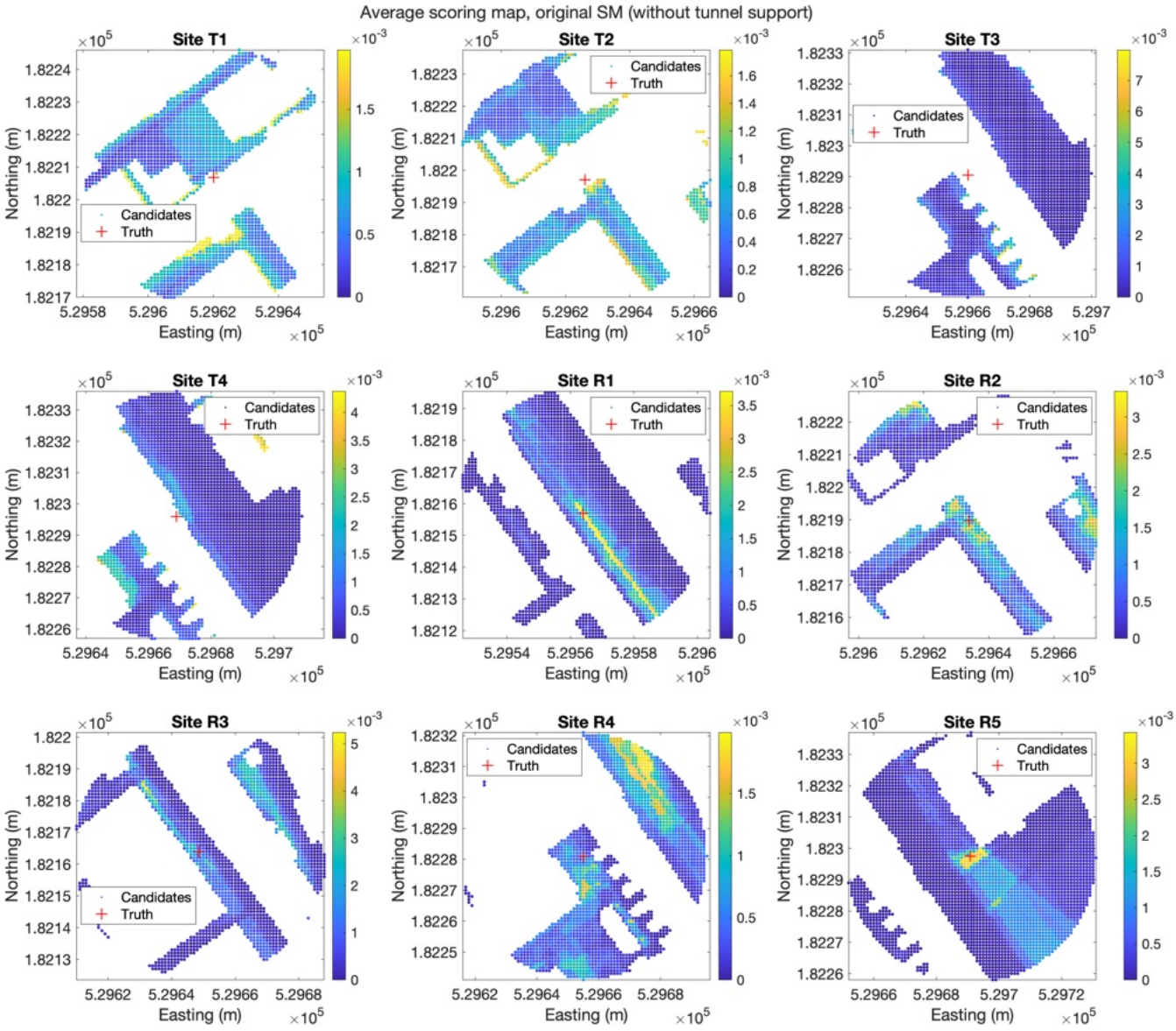

Figure 11: Average scoring map of the original SM results

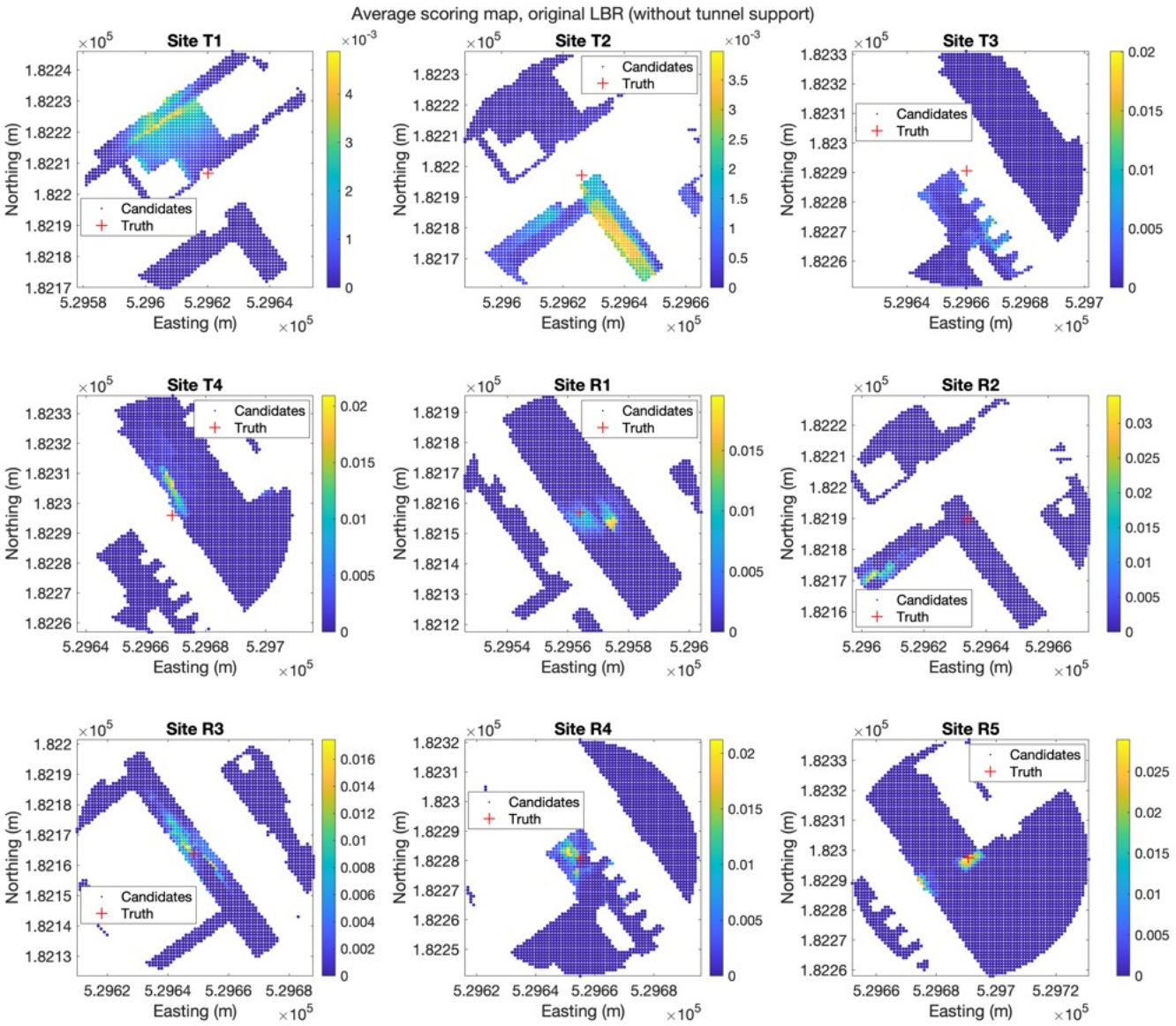

Figure 12: Average scoring map of the original LBR results

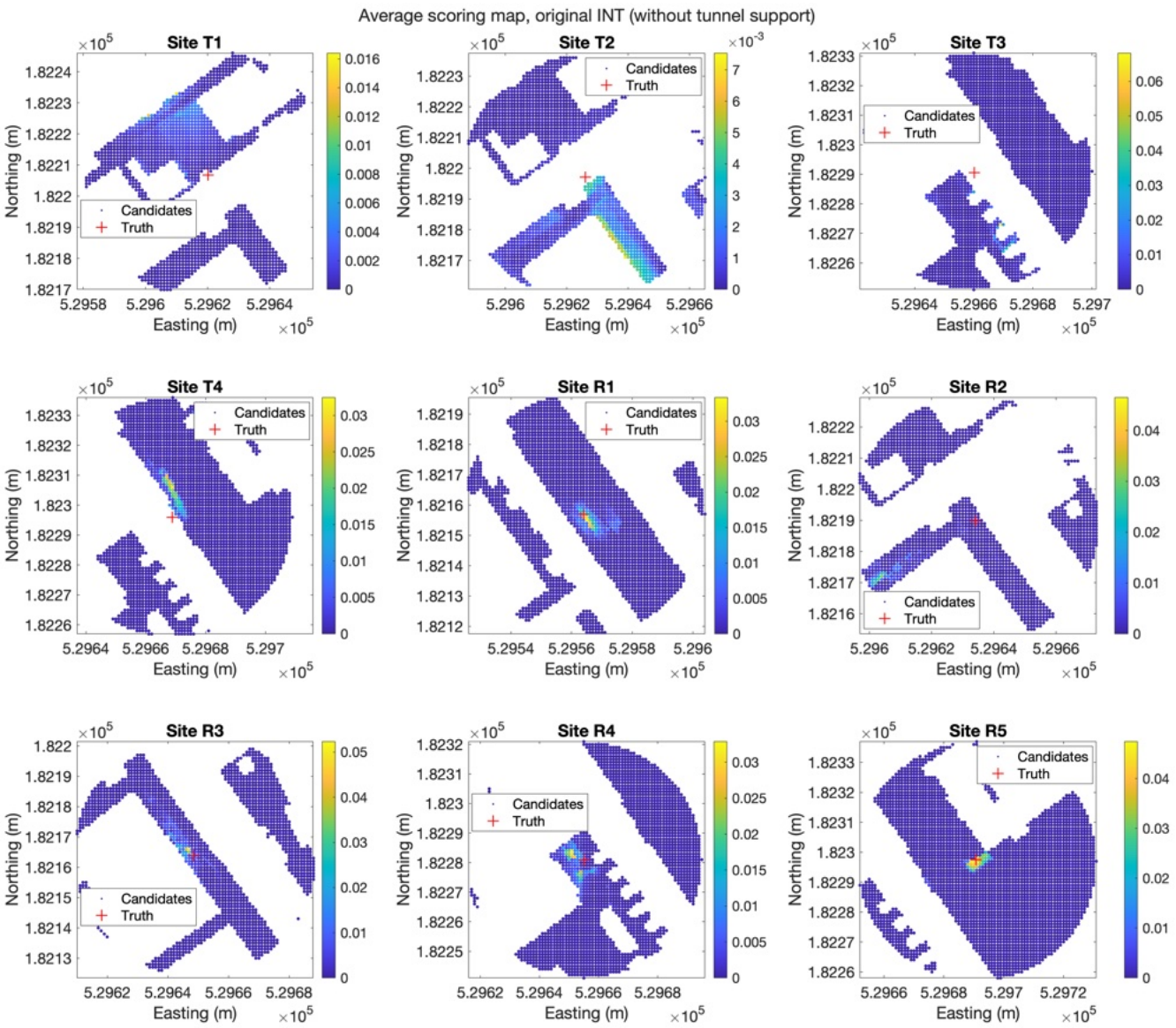

Figure 13: Average scoring map of the original integrated results

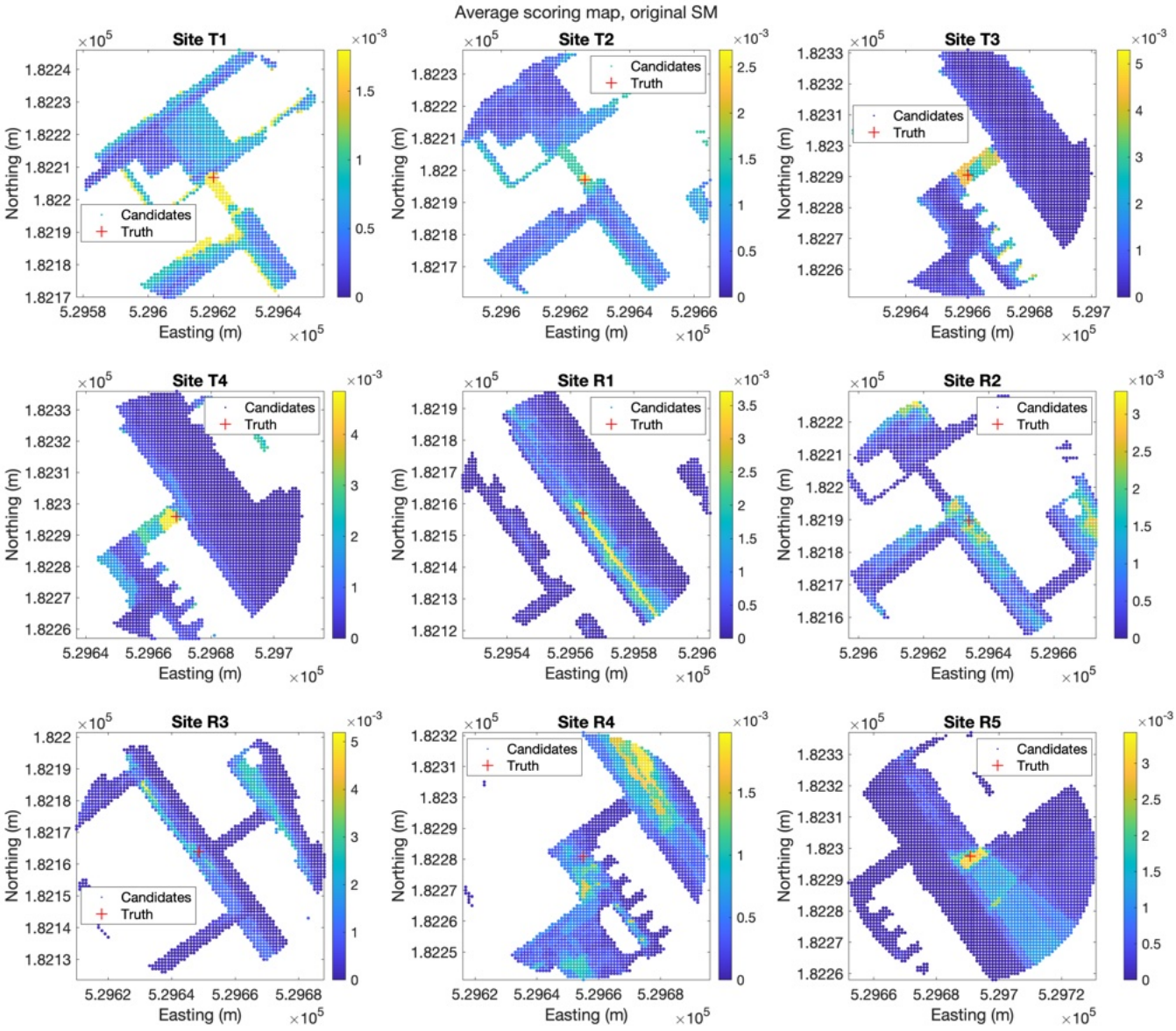

Figure 14: Average scoring map of SM results with support for tunnels

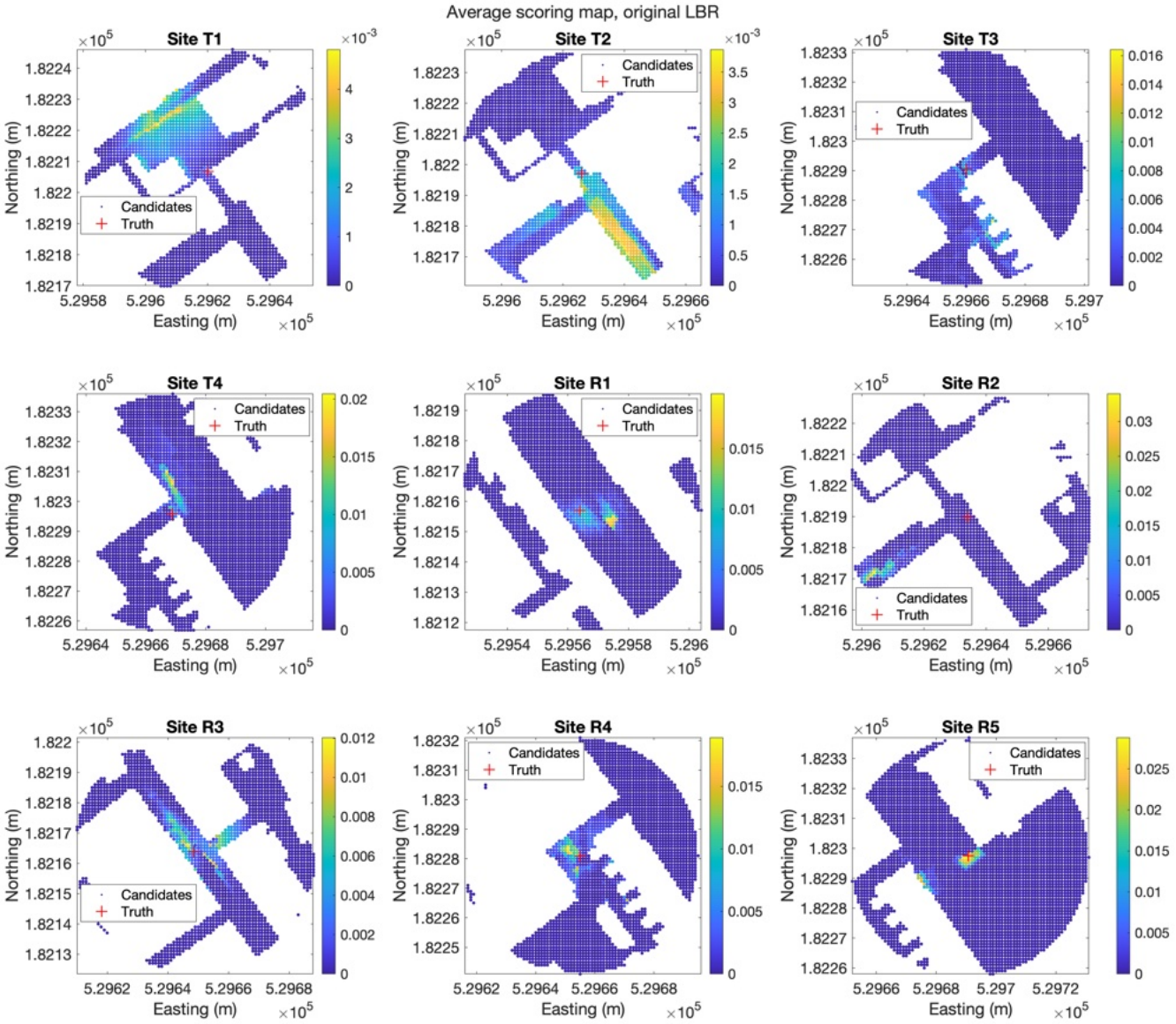

Figure 15: Average scoring map of LBR results with support for tunnels

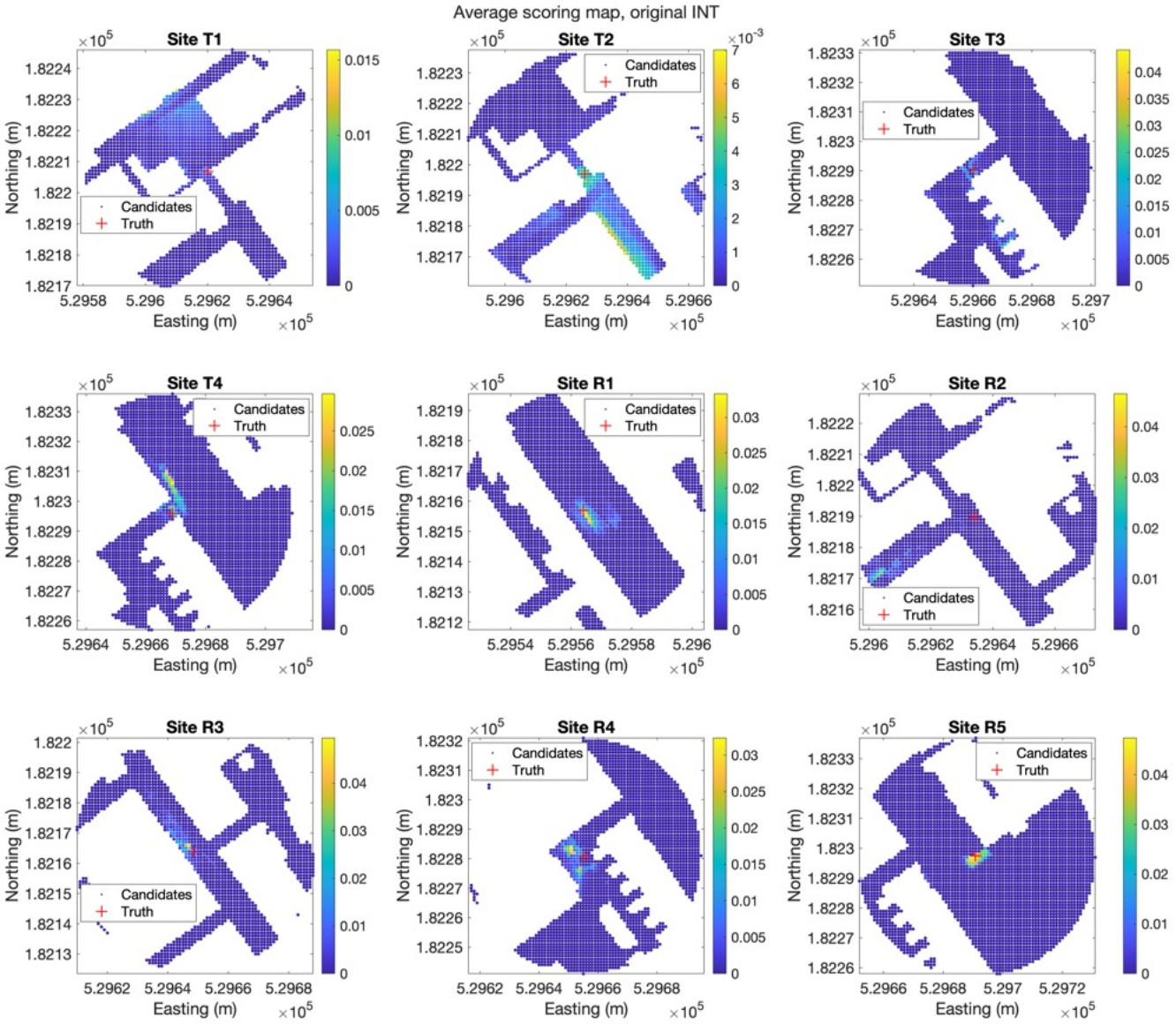

Figure 16: Average scoring map of integrated results with support for tunnels

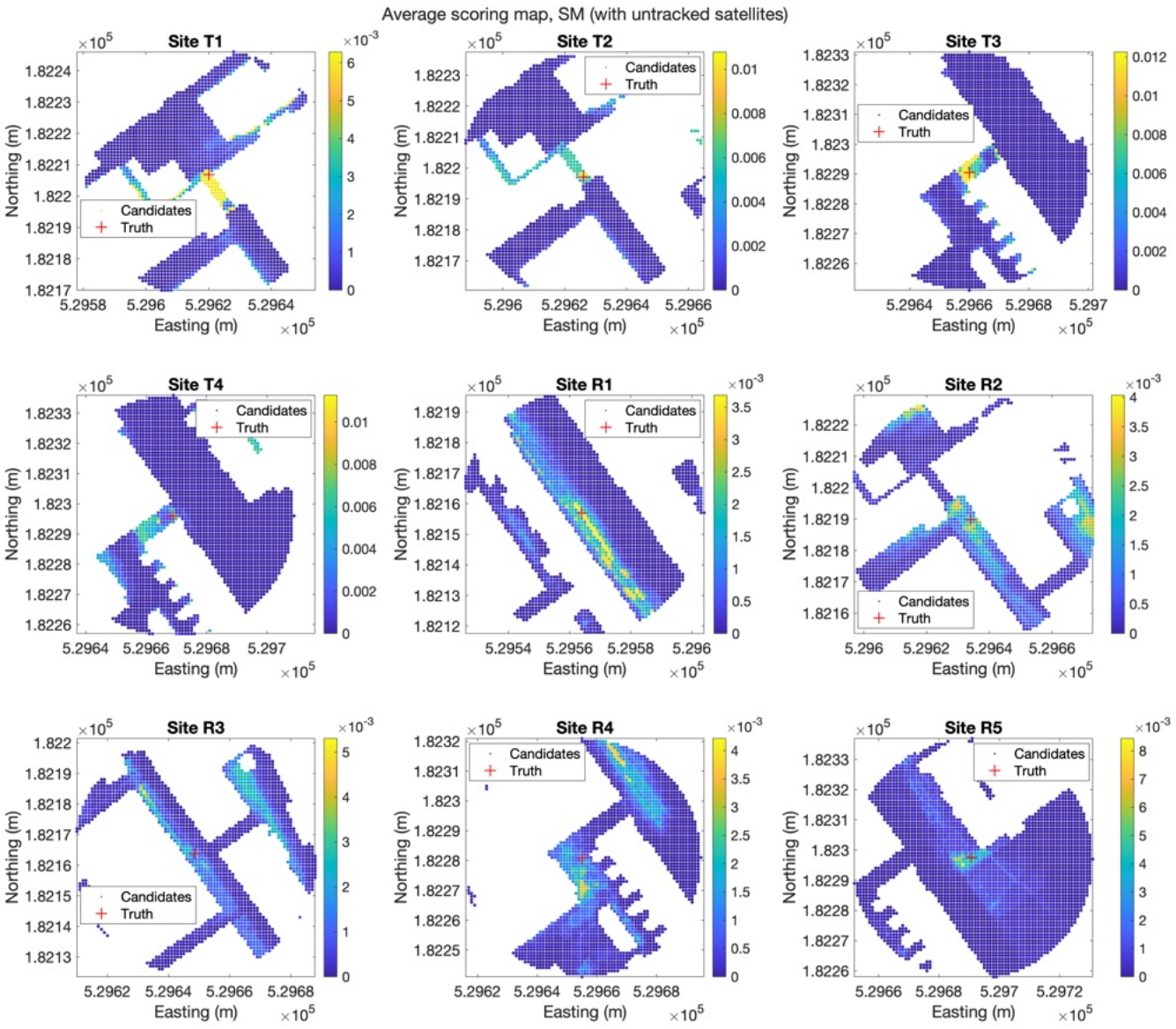

Figure 17: Average scoring map for enhanced SM results, incorporating support for tunnels and fusion of untracked satellites

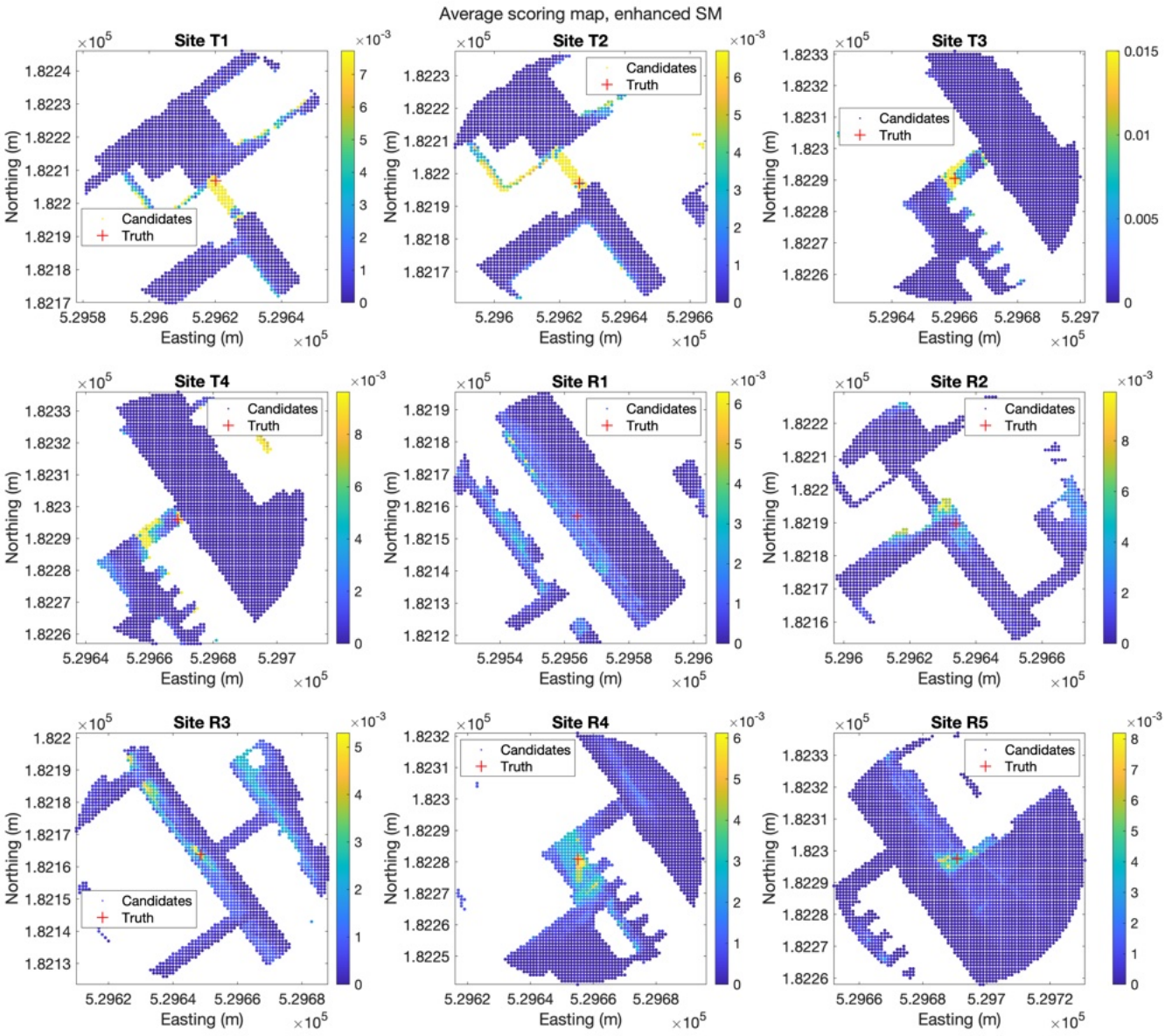

Figure 18: Average scoring map for enhanced SM results, incorporating support for tunnels, fusion of untracked satellites, and Bayesian inference

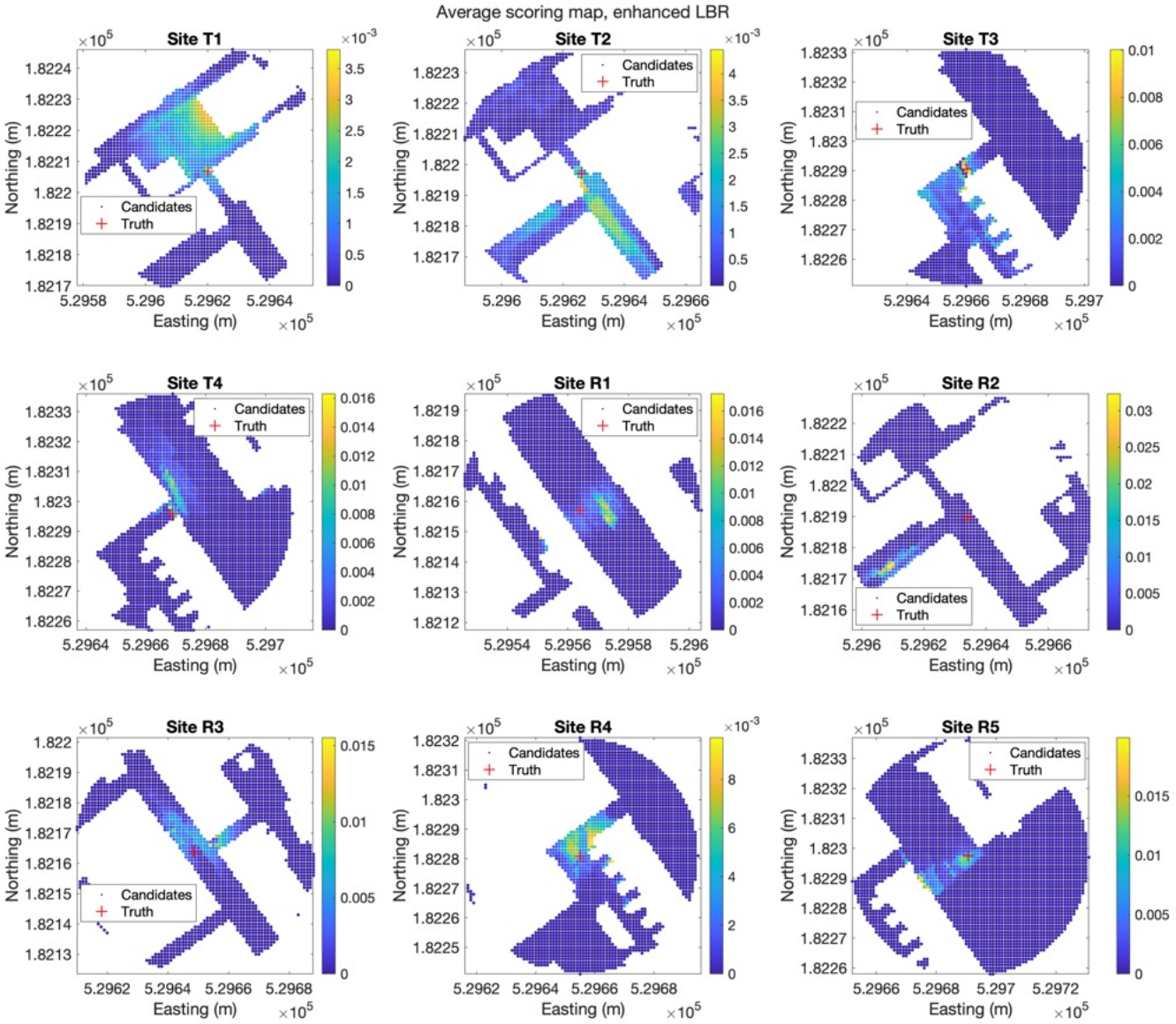

Figure 19: Average scoring map for enhanced LBR results, incorporating support for tunnels and a refined NLOS path delay model

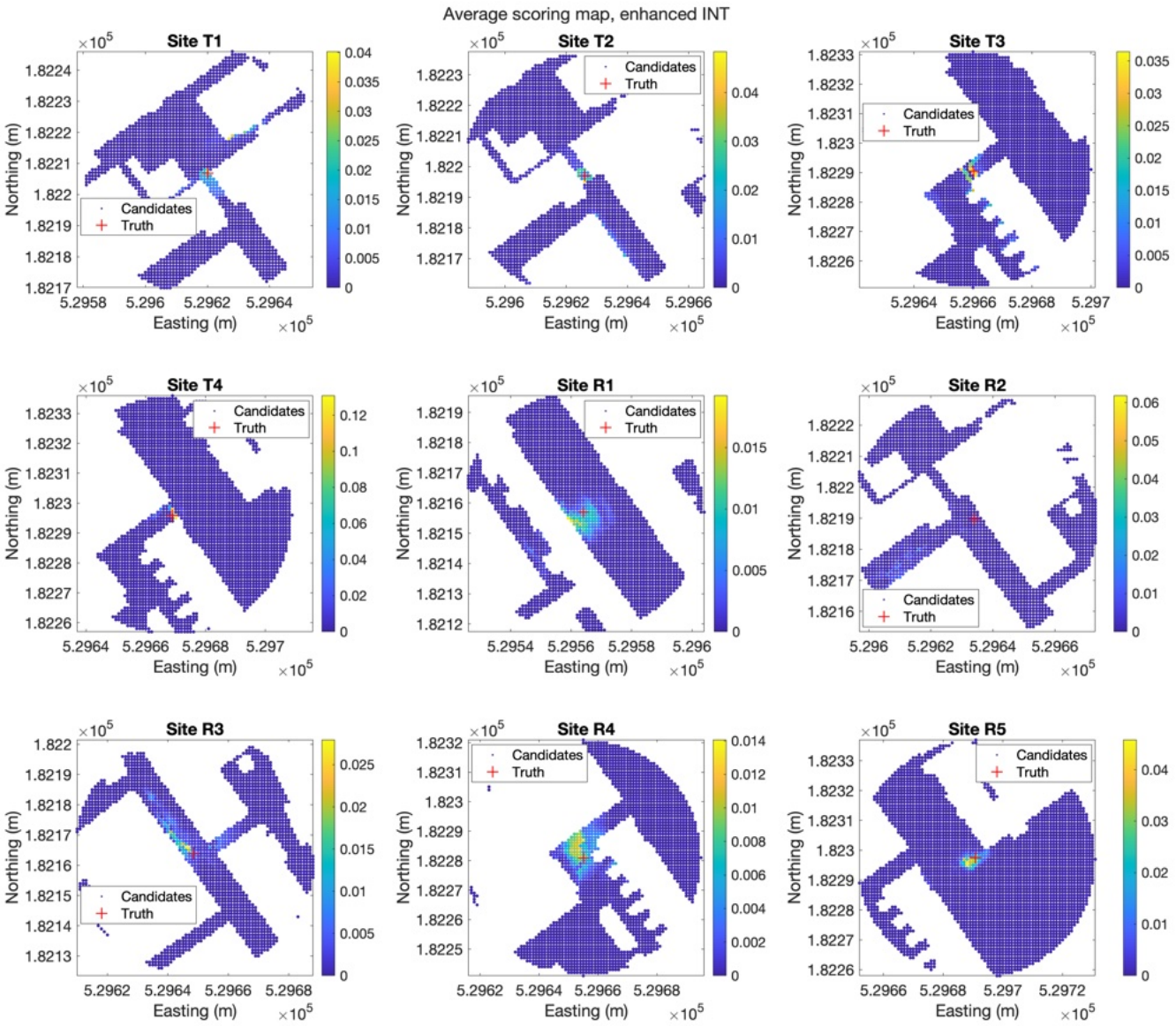

Figure 20: Average scoring map for enhanced integrated results, combining insights from the enhanced SM and LBR